A tensile ring drives tissue flows to shape the gastrulating amniote embryo

Mehdi Saadaoui, Didier Rocancourt, Julian Roussel, Francis Corson, Jerome Gros

A tensile ring drives tissue flows to shape the gastrulating amniote embryo

Mehdi Saadaoui[1,2], Didier Rocancourt[1, 2], Julian Roussel[3], Francis Corson[4]* and Jerome Gros[1,2]*

[1]Department of Developmental and Stem Cell Biology
Institut Pasteur
25 rue du Docteur Roux, 75724 Paris, Cedex 15, France

[2] CNRS UMR3738,
25 rue du Dr Roux, 75015 Paris, France

[3] Present address : Institut du Cerveau et de la Moelle épinière, Paris, France

[4] Laboratoire de Physique de l'Ecole Normale Supérieure, CNRS, ENS, Université PSL, Sorbonne Université, Université de Paris, 75005 Paris, France

* Correspondence to: corson@lps.ens.fr (FC); jgros@pasteur.fr (JG)

Abstract:
Tissue morphogenesis is driven by local cellular deformations, themselves powered by contractile actomyosin networks. Yet how localized forces are transmitted across tissues to shape them at a mesoscopic scale is still unclear. Analyzing gastrulation in entire avian embryos, we show that it is driven by the graded contraction of a large-scale supracellular actomyosin ring at the margin between the embryonic and extraembryonic territories. The propagation of these forces is enabled by a fluid-like response of the epithelial embryonic disk, which depends on cell division. A simple model of fluid motion entrained by a tensile ring quantitatively captures the vortex-like 'polonaise' movements that accompany the formation of the primitive streak. The geometry of the early embryo thus arises from a tug of war along its boundary.

One Sentence Summary:
During gastrulation, a supracellular actomyosin ring remodels the embryonic territory and shapes the primitive streak.

Main Text:

During amniote gastrulation, endodermal and mesodermal derivatives internalize through the primitive streak, a transient structure at the midline of the early embryo. In avians, the primitive streak forms from an initially crescent-shaped region at the margin between the embryo proper (EP) and extra-embryonic tissue (EE) (Fig. 1A), which converges towards and extends along the midline. While Myosin-II-driven oriented cell intercalation is known to underlie convergent extension of the prospective primitive streak (*1*, *2*), how the concomitant vortex-like tissue flows arise (*3*, *4*) and how they relate to the formation of the primitive streak has remained elusive.

To analyze gastrulation movements, transgenic quail embryos expressing a membrane-bound GFP (memGFP) (*5*) were cultured *ex vivo* (*6*) and imaged in their entirety for 12 hours. The resulting movies were processed using particle image velocimetry (PIV) to reconstruct cell trajectories and tissue deformation maps (Fig. 1B-D and Movie S1). Embryonic territories, originally characterized using anatomical or molecular criteria, could be recognized in these maps (compare Fig. 1A and 1C), and we designed automated fate mapping methods that identify and track these territories on the sole basis of tissue movement (Fig. 1E, F, Fig. S1 and Supplementary Text); validating this approach, the inferred location of the embryo margin aligned with the boundary of expression of the ectodermal/EP marker Sox3 in embryos that were fixed after live imaging (Fig. S1K, L). The angular motion of points along the margin, which wind around the EP as they converge to the posterior, captured the progress of gastrulation (Fig. 1E-G). Based on these landmarks, we registered movies of 6 embryos in space and time to construct an average embryo (Movie S2, Fig. S1 and Supplementary Text), used as a reference in the following. Importantly, the development of cultured embryos was virtually indistinguishable from an embryo imaged directly in the egg (Fig. S2 and Movie S3).

Noting that the EP maintains an approximately constant area, while the EE tissue steadily expands (Fig. 1H), we sought to distinguish area changes from other contributions to tissue movement. A decomposition into divergent (area changes) and rotational (incompressible) components indicated that gastrulation movements can be understood as the sum of three simpler flows: i) a radial, outward movement of the expanding EE tissue; ii) an area-preserving flow with two vortices within the EP; and iii) at later stages, inward movement driven by areal contraction along the streak (Fig. 1I, J and Movie S4). While large-scale flows in the epiblast have been proposed to passively ensue from the deformation of the mesendoderm (*1*, *2*, *7*), we found that rotational movement persists after the mesendodermal crescent has converged onto the midline (Fig. 1I, J), and that areal contraction makes a limited contribution to continued movement towards the streak (Fig. 1K, L) - suggesting that other forces must be at play.

For a viscous fluid that is described by the Stokes equations, these forces could be derived from the Laplacian of the velocity field (Supplementary Text). Applied to tissue flows in the epiblast, this suggested a pattern of tangential forces along the embryo margin, extending well into its anterior half (Fig. 2A and Movie S4). In the case where flow is driven by active internal stresses - here, by cell contractility -, forces inferred in this way should be understood as apparent external forces, arising from the spatial variations of the active stress. The force pattern of Fig. 2A thus pointed to a tensile margin around the EP, with a tissue-scale tension that decays from posterior to anterior; tissue along the sides of the EP is drawn towards the posterior, where tension is higher; tissue in the posterior is thrust forward, because the margin is curved (Fig. 2B). To test this hypothesis, we formulated a fluid-mechanical model that is based on the Stokes equations, with source terms for non-uniform area changes and for active tensile stresses along the margin (Fig. 2C, D and Materials and

Methods). Area changes are taken from experiment, while tensions along the margin, which moves with the tissue, are fit to the observed motion at each time step (Fig. 2C). Although strongly constrained - aside from the tensions, the initial position of the margin and its width are the only free parameters -, the model recapitulates the full course of tissue movements over 8 h (Movie S5), with > 90% accuracy for the average reference embryo (Fig. 2F, G and Materials and Methods). Based on the deformations that would result from each source term taken separately (Fig. 2E), active tensions largely account for the shaping of the embryo, while area changes are mostly responsible for EE expansion. As further abstractions, a "synthetic embryo", where the source terms are replaced by simple mathematical functions of space and time (Fig. S3, Movie S6, see also Supplementary Text, Table S1 and Fig. S4), is sufficient to quantitatively capture the movement of the tissue, and its essential features can be recovered analytically in the limit of a thin margin (Fig. S5 and Supplementary Text).

Our results so far suggested that gastrulation is best understood as a tissue-wide process, arising from a tensile margin and a fluid-like response of the epithelial epiblast, and further experiments were designed to challenge this description. First, to directly evidence a tensile margin, we performed circular UV-laser cuts (*8*) at different locations in the epiblast (Fig. 3A-C and Movie S7). Cuts along the margin revealed anisotropic tissue strains, as expected. Cuts inside the EP showed significantly lower strains, which can be ascribed to passive tissue deformation (see Supplementary Text). As a control, linear cuts at the same locations showed a strong correlation between final opening (i.e. tissue strain) and initial opening velocity (a more direct correlate of tissue stress; Supplementary Text and Fig. S7). These experiments further revealed that tension runs all the way to the anterior margin. While this could not be inferred from motion alone - motion in the model depends essentially on differences in tension-, allowing for tension in the anterior recovers patterns of shear stress that agree with the observed tissue strains (see Supplementary Text and Fig. S20B). To connect tissue-scale motion and cellular-scale behaviors, we analyzed embryos that were fixed following live imaging different time intervals (Fig. 3D-O and Figs. S8-S13). Cell segmentation of entire embryos showed a gradual increase in cell areas in the EE tissue, likely contributing to its expansion (Fig. 3E, I, K, O). Cell shapes, with an initially isotropic distribution, became elongated along the margin, consistent with a state of tension (Fig. 3F, I, L, O). Quantification of junctional phosphorylated Myosin II revealed localized myosin anisotropy, a correlate of active force generation (*9*), at the margin (Fig. 3G-I, M-O). The location of this large-scale supracellular ring aligned with the location of the embryo margin determined from the motion of the tissue before fixation, and its width agreed with that inferred from the model (Fig. S13 and Supplementary Text; see also Fig. S6). High-resolution live imaging of transgenic embryos expressing a tdTomato-MyosinII reporter revealed the progressive formation of dynamic, tangential actomyosin supracellular cables spanning 5-20 cells at the margin (Fig. S14A and Movie S8), coincident with the site of apparent forces inferred from tissue motion (Fig. S15). In the posterior margin, these cables contracted, driving oriented intercalations (*2*). In the anterior, supracellular cables were also visible but extended tangentially, concomitant with cell elongation and oriented divisions (Fig. S14B, C and Movie S9), indicative of stress dissipation (*10*). Thus, the margin exerts active tension in the posterior and passive tension in the anterior.

Second, we sought to identify the cellular basis of tissue fluidity. Since cell rearrangements contribute to stress relaxation in epithelial tissues (*11*), and since most cell rearrangements in the early avian embryo are associated with cell division (*12*), we reasoned that cell division may be required for a fluid-like behavior. Treatment with hydroxyurea (HU) efficiently suppressed cell division (Fig. S16A), but induced apoptosis on the long term (Fig. S16B). When HU was combined with the apoptosis inhibitor Q-VD-OPh, both cell division and apoptosis were suppressed (Fig. S16A, C, D) and the topology of the epithelium was

greatly stabilized compared to controls (Fig. S16E, F and Movie S10). While Q-VD-OPh alone only slightly delayed the progress of gastrulation (Figs. S1J and S17A-E), embryos incubated in both HU and Q-VD-OPh showed a dramatic slowdown by 6-8h of treatment and failed to form a primitive streak (n = 6, Fig. 4A, B, Fig. S1J, Fig. S17D, F and Movie S11). Tissue expansion persisted, but rotational movements were abolished, consistent with a suppression of fluidity (Fig. S17G and Movie S12). As a control, treatment with aphidicolin and Q-VD-OPh produced quantitatively similar results (Fig. S17H-J). Based on the model, the amplitude of the tension/viscosity ratio dropped over time (Fig. 4C). Laser cuts in embryos treated with HU and Q-VD-OPh revealed that tensions were still present, if not increased, along the margin (Fig. S17K-M and Movie S13), and a supracellular ring was still observed in fixed embryos (Fig. 4D and Fig. S18) - implying that the slowdown resulted from an increase in viscosity and not from a decrease in tension. Thus, fluidity of the embryonic epithelium is required for primitive streak formation and emerges from cell division.

Third and finally, we challenged model predictions for hydrodynamic effects in gastrulation. The embryo, which draws the surrounding tissue to the posterior, is akin to a swimmer, and should move forward over time. Indeed, embryos exhibited a slow anterior-ward movement, in quantitative agreement with the model (Fig. S19). At odds with the view that vortex-like flows are shaped by a confining boundary (*7*, *13*, *14*), our model suggests that they are governed by the distribution of active forces, with boundary conditions playing a limited role in the intact epiblast. The progress of gastrulation is predicted to be weakly sensitive to the distance to epiblast border, reaching > 80% of its maximum rate when it is just 50% larger in radius than the EP (Fig. S4D and Supplementary Text). Indeed, circular cuts centered on the margin, that removed most of the EE tissue and brought the epiblast border closer to the EP, had almost no effect on tissue flow and streak formation (Fig. 4E, F and Movie S14). By contrast, in the case of off-centered cuts, which bring the border even closer to one side of the EP, the model predicted, and experiments confirmed, that the interaction between EP and border induces a rotation of the axis, leaving only one apparent vortex, and resulting in a bent streak (Fig. 4G, H and Movie S14).

Our study demonstrates the power of fluid-mechanical approaches (*9*, *15*, *16*) to capture large-scale morphogenetic movements, and identifies a simple mechanical basis for gastrulation. While tissue-wide flows in the embryonic disk were previously interpreted as a passive consequence of primitive streak formation (*1*, *2*, *7*), we find instead that both are part of a broader process, that is driven by tensile forces all along the margin and shapes the embryo as a whole (see Supplementary Text and Fig. S20 for further discussion of alternative models). Supracellular actomyosin cables, which have been shown to drive local cell rearrangements, stabilize compartment boundaries, and act as purse strings in wound healing and embryonic tissue closure (*17*, *18*), effect here a large-scale remodeling of the surrounding tissue through non-uniform contraction. Our finding that the embryo margin, previously identified as a molecular organizer of early development (*19–21*), is also defined by a specific mechanical state and cellular behaviors, hints that mechanical and molecular cues may combine in the establishment of the amniote body plan.

References:

1. O. Voiculescu, F. Bertocchini, L. Wolpert, R. E. Keller, C. D. Stern, *Nature*. **449**, 1049–1052 (2007).
2. E. Rozbicki *et al.*, *Nat. Cell Biol.* **17**, 397–408 (2015).
3. R. Wetzel, *Wilhelm Roux Arch. Für Entwicklungsmechanik Org.* **119**, 188–321 (1929).
4. L. Gräper, *Dev. Genes Evol.* **116**, 382–429 (1929).
5. C. Moreau *et al.*, *Curr. Biol. CB.* **29**, 35-50.e4 (2019).

6. S. C. Chapman, J. Collignon, G. C. Schoenwolf, A. Lumsden, *Dev. Dyn. Off. Publ. Am. Assoc. Anat.* **220**, 284–289 (2001).
7. O. Voiculescu, L. Bodenstein, I.-J. Lau, C. D. Stern, *eLife*. **3**, e01817 (2014).
8. I. Bonnet *et al.*, *J. R. Soc. Interface*. **9**, 2614–2623 (2012).
9. S. J. Streichan, M. F. Lefebvre, N. Noll, E. F. Wieschaus, B. I. Shraiman, *eLife*. **7**, e27454 (2018).
10. P. Campinho *et al.*, *Nat. Cell Biol.* **15**, 1405–1414 (2013).
11. C. Guillot, T. Lecuit, *Science*. **340**, 1185–1189 (2013).
12. J. Firmino, D. Rocancourt, M. Saadaoui, C. Moreau, J. Gros, *Dev. Cell*. **36**, 249–261 (2016).
13. M. Chuai, C. J. Weijer, in *Current Topics in Developmental Biology*, P. K. M. Santiago Schnell, Ed. (Academic Press, 2008; http://www.sciencedirect.com/science/article/pii/S0070215307810040), vol. Volume 81, pp. 135–156.
14. S. A. Sandersius, M. Chuai, C. J. Weijer, T. J. Newman, *Phys. Biol.* **8**, 045008 (2011).
15. B. He, K. Doubrovinski, O. Polyakov, E. Wieschaus, *Nature*. **508**, 392–396 (2014).
16. M. Smutny *et al.*, *Nat. Cell Biol.* **19**, 306–317 (2017).
17. K. Röper, *Bioarchitecture*. **3**, 45–49 (2013).
18. C. Schwayer, M. Sikora, J. Slováková, R. Kardos, C.-P. Heisenberg, *Dev. Cell*. **37**, 493–506 (2016).
19. K. Joubin, C. D. Stern, *Cell*. **98**, 559–571 (1999).
20. R. F. Bachvarova, I. Skromne, C. D. Stern, *Dev. Camb. Engl.* **125**, 3521–3534 (1998).
21. S. B. Shah *et al.*, *Dev. Camb. Engl.* **124**, 5127–5138 (1997).

Acknowledgments: We thank Vincent Hakim, Pierre-Francois Lenne, Alfonso Martinez Arias, and François Schweisguth for critical reading of the manuscript and Paolo Caldarelli for the *in situ* hybridization in Fig. S1K, L.

Funding: The research leading to these results has received funding from the European Research Council under the European Union's Seventh Framework Programme (FP7/2007-2013) / ERC Grant Agreement *n°337635*, from the Institut Pasteur, the CNRS, the Cercle FSER, the Fondation pour la Recherche Medicale and the Vallee Foundation.

Author contributions: M.S., F.C. and J.G. conceived the study. D.R. and J.R. generated transgenic lines. M.S. performed experiments. F.C. developed quantitative analysis methods and theoretical models. F.C. and J.G. wrote the paper with input from M.S.

Competing interests: Authors declare no competing interests.

Data and materials availability: All data is available in the main text or the supplementary materials.

Supplementary Materials:
Materials and Methods
Supplementary Text
Figures S1-S20
Table S1
Movies S1-S14
References (*22*–*38*)

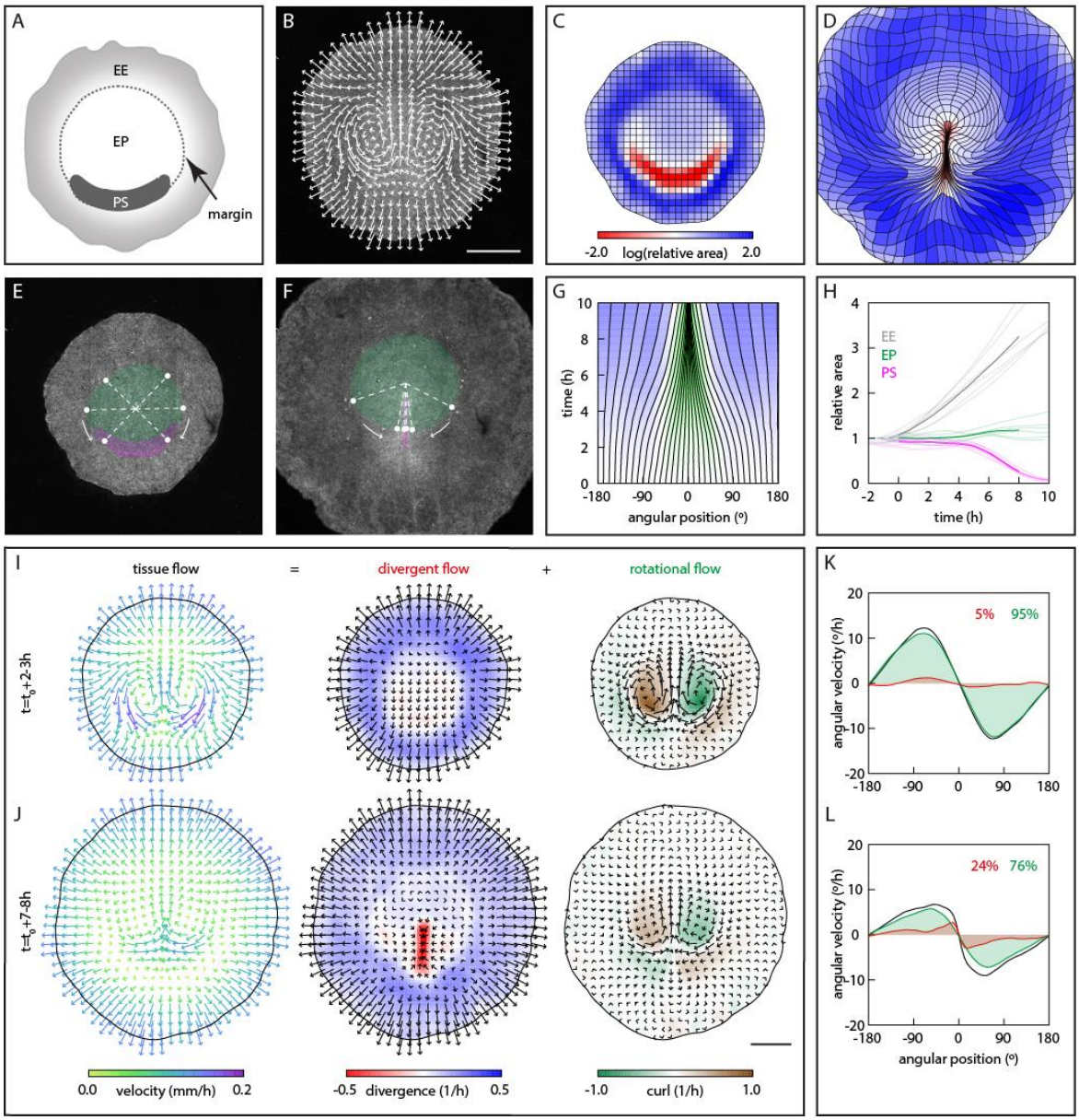

Fig. 1. Quantitative description of gastrulation movements.
(**A**) Early epiblast. (**B**-**D**) Trajectories (**B**, *t* = 4-6 h) and deformation of an initially square grid (**C**, **D**), from the PIV analysis of a memGFP embryo movie (colors in **C**, **D** show area changes between the initial (**C**, *t* = 0) and final (**D**, t = 10 h) configurations). (**E**-**H**) Automated fate mapping (green, EP; magenta, primitive streak, PS); dots show winding motion (arrows) along the margin, quantified in **G** by the time evolution of angular positions (dotted lines in **E**, **F**; 0º is posterior); **H**, area of tissue regions vs. time (*n* = 6 embryos; bold lines, averages). (**I**-**L**) Decomposition of the tissue velocity field into divergent and rotational components (**I**, **J**), and contributions to motion along the margin (**K**, **L**; colors as in **I**; percentages quantify shaded areas) (averages over *n* = 6 embryos and the indicated time intervals). t_0, time of motion onset. Scale bars, 1 mm.

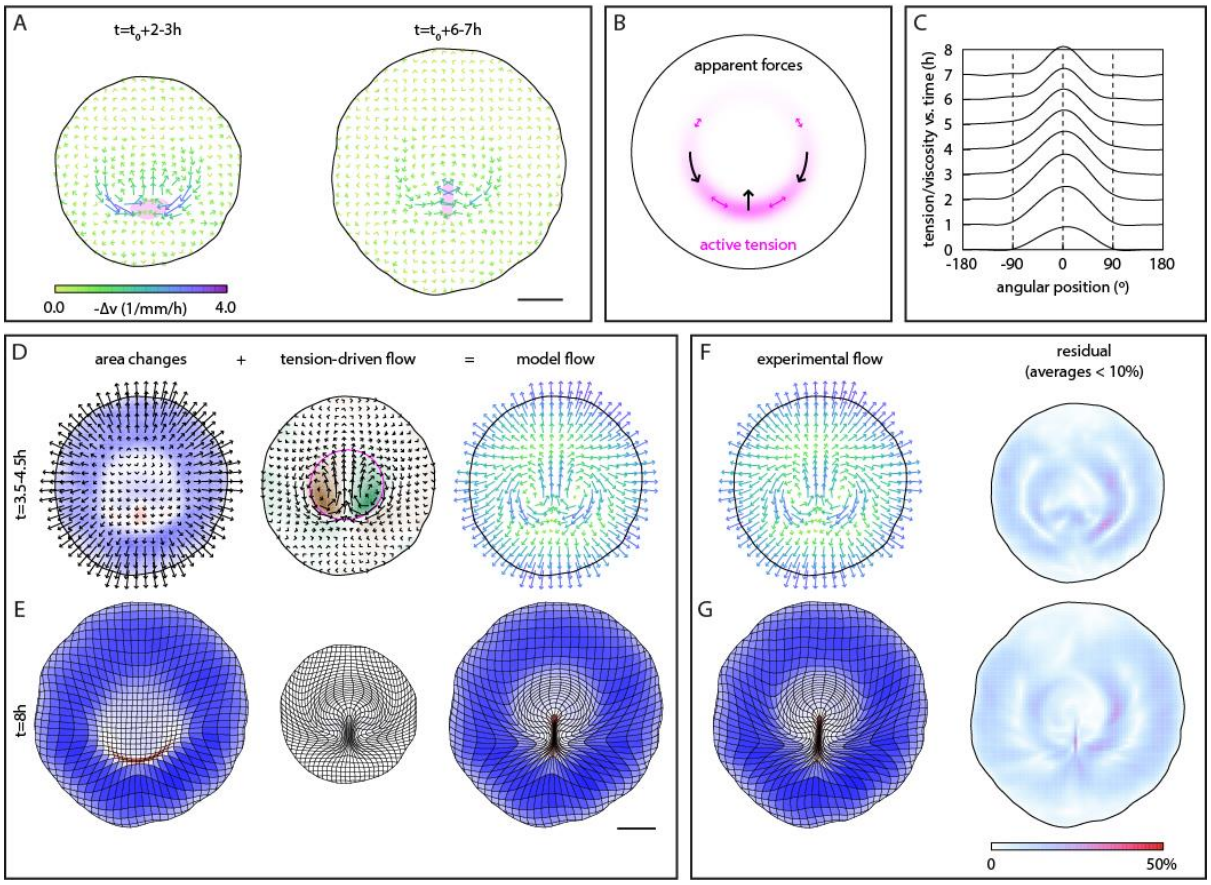

Fig. 2. A quantitative fluid-mechanical model for gastrulation.
(**A**) Apparent forces (negative of the Laplacian of the velocity field; averages over $n = 6$ embryos; magenta, presumptive primitive streak). (**B**) Sketch illustrating how apparent forces (black) arise from graded tensions along the margin (magenta). (**C-E**) Quantitative model for gastrulation movements. **C**, Tension/viscosity profiles (mm/h; averages over 1 h intervals) from a fit to the reference average embryo ($n = 6$ embryos). **D**, **E**, Tissue flows in the model as the resultant of area changes (taken from experiment) plus an incompressible flow driven by tension along the margin (magenta line in **D**). **D**, Velocity fields (colors as in Fig. 1I). **E**, Deformation maps from each source term taken separately and together. (**F-G**) Velocity field (**F**) and deformation map (**G**) for the average embryo (right-hand panels show deviation between model and experiment). Scale bars, 1 mm.

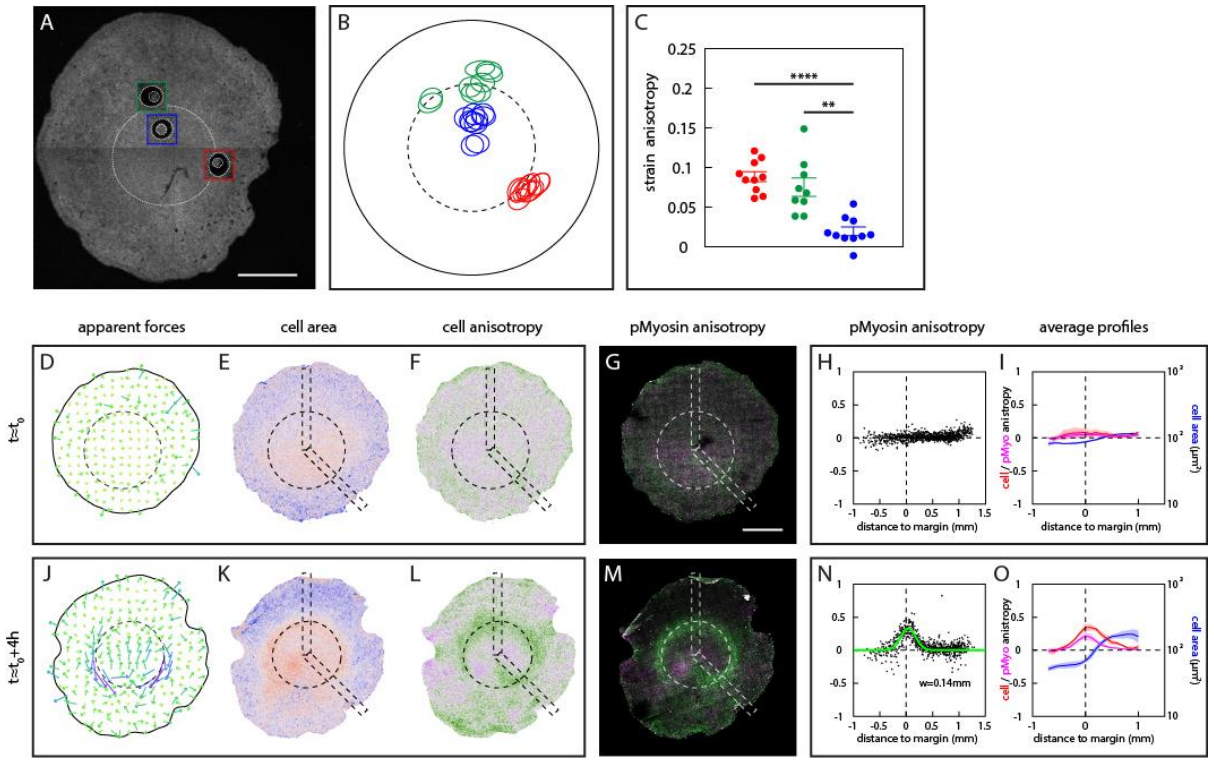

Fig. 3. Mechanical, cellular, and molecular characterization of the embryo margin. (**A**-**C**) 250 µm circular laser cuts in a single memGFP embryo (**A**) and representation of all laser cut experiments (**B**; ellipses show anisotropic strain amplified 4-fold for visibility) (**C**; tangential vs. radial strain anisotropy; bars, mean ± SE; ** P<.01; **** P<.0001; paired t-test) (red, posterior margin; green, anterior margin; blue, EP). (**D**-**O**) Apparent forces (**D**, **J**) in embryos imaged until indicated stages (dashed line, margin), and cell areas (**E**, **K**), cell shape anisotropy (**F**, **L**), and junctional phosphorylated Myosin anisotropy (tangential, green, vs. radial, magenta, in **G**, **M** and averaged in 100×100 µm boxes in **H**, **N**) mapped in these embryos and averaged across embryos (**I**, **O**; mean ± SE of radial profiles in n = 2 and n = 3 embryos). Boxed regions are shown in Figs. S8-S11 and individual embryos from **I**, **O** in Figs. S12 and S13. Green curve in **N**, Gaussian fit with standard deviation *w*, as indicated. Scale bars, 1 mm.

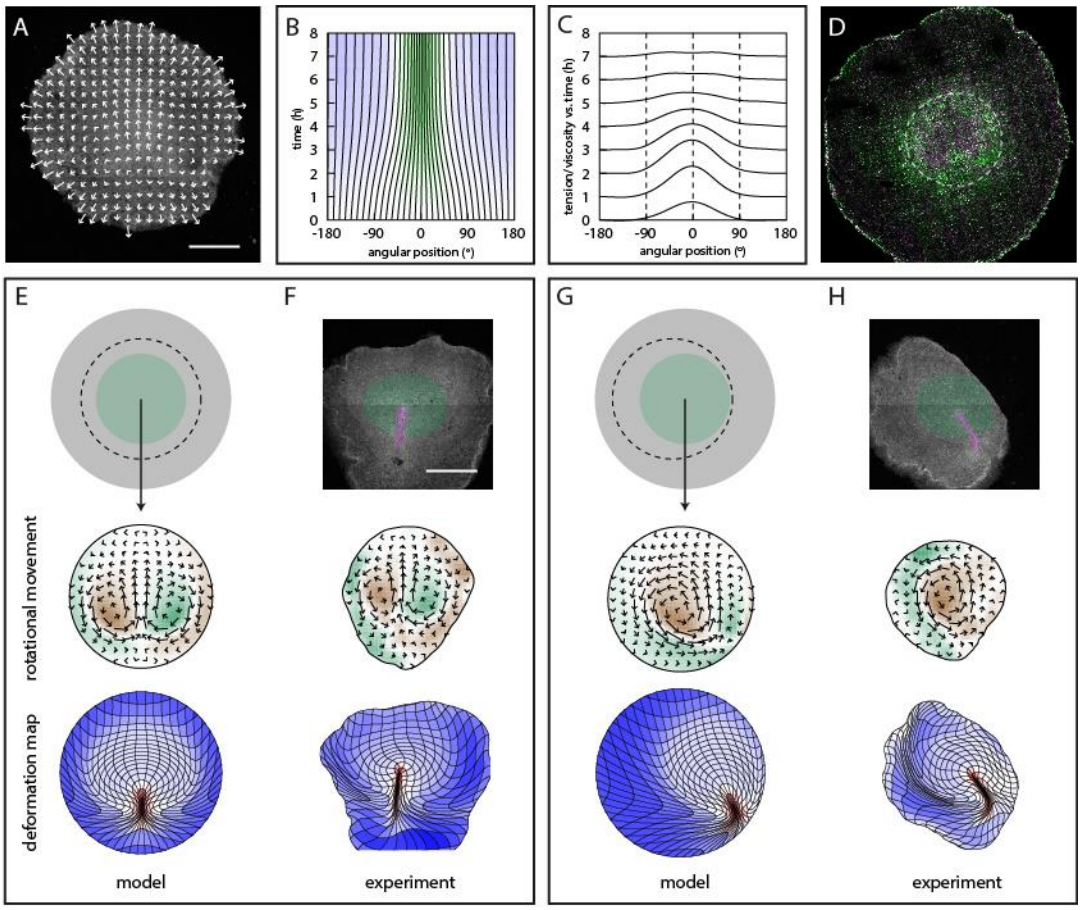

Fig. 4. Manipulation of tissue viscosity and hydrodynamic effects in gastrulation. (**A**-**D**) Effect of HU+Q-VD-OPh on gastrulation movements (n = 5 embryos). **A**, Trajectories (individual embryo, t = 4-6 h). **B**, Time evolution of angular positions along the margin (average embryo). **C**, Tension/viscosity profiles from model fit to average embryo. **D**, Junctional phosphorylated Myosin anisotropy (cf. Fig. 3M). (**E**-**H**) Predictions from the synthetic model (**E**, **G**) and experimental response to centered (**F**) and off-centered (**H**) cuts generating a new tissue border. Scale bars, 1 mm.

Supplementary Materials for

A tensile ring drives tissue flows to shape the gastrulating amniote embryo

Mehdi Saadaoui, Didier Rocancourt, Julian Roussel, Francis Corson and Jerome Gros

Correspondence to: corson@lps.ens.fr (FC); jgros@pasteur.fr (JG)

This PDF file includes:

Other Supplementary Materials for this manuscript include the following:

Materials and Methods

Animals

All experimental methods and animal husbandry procedures to generate transgenic quails were carried out in accordance with the guidelines of the European Union 2010/63/UE.

Production and characterization of transgenic quail lines

Two transgenic lines were created in this study (*hUbC:memGFP* and *hUbC:Lifeact-NeonGreen-ires-Myl9-tdtomato)* by following a previously published method (*22*). Briefly, non-incubated quail eggs (*Coturnix japonica*) were windowed and a solution of high titer lentivirus was injected into the subgerminal cavity of stage X embryos. Eggs were sealed with a plastic piece and paraffin wax. Injected eggs were incubated at 37.5°, 56% humidity until hatching. For the *hUbC:memGFP* line, a total of 42 embryos were injected with the lentivirus solution (titer 10^{10}/ml). Three F0 mosaic founder males successfully hatched and reached sexual maturity (7%). They were bred to WT females and all three produced transgenic offspring (transmission rate: 8.8%). One line was selected on the basis of a single copy of the transgene, checked by Southern Blot, and high intensity of the memGFP signal. For the *hUbC:Lifeact-NeonGreen-ires-Myl9-Tdtomato*, a total of 92 embryos were injected with the lentivirus solution (titer 4.5 10^7/ml). Four F0 mosaic founder males hatched, reached sexual maturity (4%) and were bred to WT females. One line with a single copy of the transgene was segregated, by Southern Blot analysis, from a line presenting three copies of the transgene and a high intensity of the tdTomato signal.

Embryo culture, time-lapse microscopy and laser severing experiments

Transgenic quail eggs were collected at stage XI and cultured using a modified version of the EC culture system (*4*) until stage 4. Briefly, embryos were collected using paper filter rings and cultured on mix of albumen, agarose (0.2%), glucose, and NaCl. Embryos were then transferred into a bottom glass Petri dish (Mattek inc.) with semi solid albumen/agarose nutritive substrate with or without drugs: HydroxyUrea (40mM), Q-VD-OPh (250µM-1mM) for imaging. Embryos were then imaged at 38°C using an inverted confocal microscope (Zeiss LSM 880 or LSM 700) or a 2-photon Microscope (Zeiss, NLO LSM 7MP) coupled to a Chameleon Ti/Saph femtosecond pulsed laser (Coherent inc.) at 840nm wavelength using 5X, 10X or 40X long distance objectives.

Laser microdissections were performed during image acquisition using a 355-nm pulsed laser (75-100% power), a UGA-42 module from Rapp Optoelectronic coupled to a Zeiss LSM 880 and a 5X or 10X objective. Before and after severing, the time interval between two consecutive frames was 6 min. Briefly, a PIV analysis as described below, and the pattern of apparent forces inferred from tissue motion (cf. Fig. 2A), was used to locate the embryo margin and define ROIs of different sizes in order to isolate the embryonic region (from 1.8mm to 2.5mm) or to probe the tension at different locations within the epiblast (between 250 and 500µm). In the case of circular cuts, images were acquired during severing every 5s, and the tissue strain was evaluated based on the deformation of the tissue 2 min after the cut, from a PIV analysis of the resulting time-lapse movies; in the case of linear cuts, images were acquired every second to track the opening of the cut (see Supplementary Text for details). A posteriori, automated fate mapping as described below was applied to movies acquired before severing to confirm the location of the cuts relative to the margin (as displayed in Fig. 3A), and to movies acquired after severing to locate the EP and primitive streak in isolated portions of the epiblast (as displayed in Fig. 4F, H).

Quantitative analysis of tissue flows

Following a common approach to describe the morphogenesis of epithelial sheets (*9*, *16*, *23*), the motion of the planar epiblast was described as a continuous, two-dimensional flow field. Within this description, the out-of-plane motion of ingressing mesensodermal cells, which leave the epiblast, contributes to areal contraction of the tissue. Time-lapse movies of embryos were analyzed using custom Java software, building on the ImageJ API for image processing. The full details of processing and analysis are given in Supplementary Text. Briefly, particle image velocimetry (PIV) was used to evaluate the local displacement of the tissue between successive movie frames. The resulting displacement fields were used to reconstruct cell trajectories, and a family of mappings that relate the configuration of the tissue at any two time points. In terms of these mappings, deformation maps as in Fig. 1D show the image of an initially square grid at a later time.

Tissue velocity fields were decomposed into a divergent, approximately irrotational component, and a divergence-free, rotational component using a variation on the Helmoltz-Hodge decomposition of vector fields, adapted such that the divergent component coincides with the full velocity field at the tissue border (this implies that, in general, the divergent component is not exactly irrotational).

Automated fate mapping and spatiotemporal registration

The location of the embryo margin was identified using an active contour or "snake" approach (*24*); as a first step, we constructed a function of space that changes sign across the margin, based on the distinctive tissue deformation patterns observed on either side. The primitive streak was identified from the pattern of areal contraction in the tissue, by thresholding. The orientation of the posterior was identified as a fixed point in the angular motion of points along the margin. Embryos were registered in space based on the location of the margin, and in time based on the time of motion onset and the time of streak formation, both defined according to the angular contraction of an initially 90º sector centered on the posterior (see Supplementary Text for details).

Fluid-mechanical model

The full details of model derivation, simulation, fitting, and analysis, are given in Supplementary Text. Briefly, the tissue is treated as effectively incompressible, and areal expansion or contraction as intrinsic behaviors of different tissue regions, akin to growth. We note that this choice is not meant to imply that these behaviors are actually insensitive to mechanical stresses, but as a mathematical simplification, allowing us to incorporate tissue area changes without addressing their regulation, which like the regulation of active stresses at the margin, lies beyond the scope of the present study. Taking the long-time limit of a viscoelastic description of the tissue, we recover the Stokes equations for viscous flow, with an additional source term for areal expansion or contraction,

$$\eta \nabla^2 \mathbf{v} - \nabla P + \nabla \cdot \sigma_a = 0 \qquad \text{(S1)}$$

$$\nabla . \mathbf{v} = \gamma \qquad \text{(S2)}$$

Equation (S1), with $\mathbf{v}$ denoting the velocity, η the viscosity, P the pressure, and σ_a an active internal stress tensor, expresses force balance, and is unchanged from the incompressible fluid

case. In equation (S2), the usual incompressibility condition $\nabla \cdot \mathbf{v} = 0$ is replaced by a prescribed divergence g, corresponding to the local rate of areal expansion or contraction. Area changes and the motion of the tissue border, which defines the boundary condition of the model, are taken from experiment (from an individual or average embryo). The active internal stress takes the form of a tensile stress along the margin, represented by a contour that is advected with the tissue. The tensile stress has a Gaussian profile across the width of the margin, and its magnitude at different positions along the margin is represented by the total tension across the width of the margin. For an approximately circular margin, the average tension has almost no incidence on motion, and it is arbitrarily chosen such that the tension vanishes in the anterior. Tension profiles at each time step are fit to the observed tissue motion, leaving the initial position of the margin and its width as fitting parameters. The source term for area changes, g, is computed from the observed tissue flow in two different ways. In the simplest, "Eulerian" treatment, it identifies with the divergence of the observed velocity field, and the divergent component of the model flow coincides with its experimental counterpart. In a refined, "Lagrangian" treatment, the rate of areal expansion or contraction is a property of material points in the tissue, and thus tied to the initial, rather than the current configuration of the tissue. The "Eulerian" treatment is used for parameter fitting. The "Lagrangian" model, which is computationally more expensive, is simulated with the resulting parameter values, as the definitive form of the model.
The synthetic model is obtained by replacing the source terms - area changes and tensions - by analytical functions of space and time. As a boundary condition, the tissue border is circular and moves outwards at a uniform velocity, determined at each time step according to the integrated area change. The resulting model, which is left-right symmetric by construction, was fit and compared to a symmetrized average embryo, obtained by including a mirror image of each embryo.

Model residual

Two measures of the deviation between model and experiment were used. A normalized step-by-step residual, used to define the reported accuracy of the main model, is obtained as the magnitude (the L^2 norm) of the deviation between the displacement fields at each time step in model and experiment, $d\mathbf{r}$ and $d\mathbf{r}_{\mathrm{exp}}$, divided by the magnitude of the experimental displacements,

$$\sqrt{\frac{\sum_i \left| d\mathbf{r}_{\mathrm{exp}}(t_i,t_{i+1}) - d\mathbf{r}(t_i,t_{i+1}) \right|^2}{\sum_i \left| d\mathbf{r}_{\mathrm{exp}}(t_i,t_{i+1}) \right|^2}} \qquad \text{(S3)}$$

A normalized end-to-end residual, displayed in Fig. 2G and Fig. S3B, is defined in the same way from the displacements between the initial and final time points,

$$\frac{\left| d\mathbf{r}_{\mathrm{exp}}(t_1,t_n) - d\mathbf{r}(t_1,t_n) \right|}{\left| d\mathbf{r}_{\mathrm{exp}}(t_1,t_n) \right|} \qquad \text{(S4)}$$

Step-by-step residuals for $n = 6$ control embryos, evaluated using 1 h steps to limit the contribution of fluctuations, ranged from 10.4 to 15.5%. For the average reference embryo, it was under 10%.

Analysis of cell behaviors and fixed embryos

Time-lapse movies were analyzed using Fiji(*25*) and Icy software. Quantifications were performed manually on registered movies (*26*) by visual inspection. For cell division quantification, ROIs from at least 3 independent experiments were used to count the number of dividing cells in the first 5-6h of the movies. For epithelial stability in different conditions (ctrl, HU, HU+Q-VD-OPh, and Q-VD-OPh) and after a step of image segmentation (described below), the Epitools (*27*) plugin for Icy (*28*) was used to generate the movies with the cell color tag option in the cell overlay panel.

For fixed samples, optical sections were obtained on a confocal microscope (LSM700 or LSM880; Zeiss) using a 40X (C-Apochromat NA 1.1 water immersion) objectives and Zen software (Zeiss). Images were analyzed using Fiji and Icy softwares.

For segmentation, the apical signal was first extracted from image stacks using a custom program that fits a smooth surface to the tissue. After image processing, a binary mask was generated using the Find Maxima tool of Fiji and then subjected to manual correction using Tissue Analyzer (*29*). The segmented images were then analyzed as described in Supplementary Text.

Immunofluorescence and in situ hybridization

For antibody stainings, quail embryos were fixed in ice cold 4% formaldehyde/PBS for at least 1h, permeabilized in PBS/0.1% Triton X-100 (PBT 0.1%) before a blocking step in PBT 0.1%/2% BSA (from Roche)/10% FBS (from Gibco). Primary antibodies used in this study are mouse anti-ZO1 (Invitrogen ZO1-1A12), rabbit anti-pMyosin light chain 2 (Cell Signaling Technology CST-3671S and CST-3674S), mouse anti-β-Catenin (BD Transduction Laboratories™, clone 14) and rabbit anti-h/mCaspase3 (RD Systems AF835). Secondary antibodies coupled to AlexaFluor 488, 555, or 647 were obtained from Invitrogen and used at 1:200 dilutions. Embryos were then mounted with DAPI-containing Fluoromount-G™ (eBioscience) between slide and coverslip.

In situ hybridization was performed as described previously (*3*), using a probe against Sox3, a kind gift from Angela Nieto.

Supplementary Text

S1. Quantification of tissue flows

Tissue movement was quantified using Particle Image Velocimetry (PIV) (*30*). Movies frames were first filtered using ImageJ's Normalize Local Contrast plugin, with a spatial scale ≈ 7.5μm, to minimize the effect of imaging defects such as dark spots while preserving cell-scale detail. As an alternative to identifying and replacing spurious displacement vectors, the displacement vectors are computed by minimizing a global cost function, with a regularization term that penalizes sharp variations between adjacent interrogation windows. This approach has the benefit of preserving the information present in areas where the image has an anisotropic correlation structure. The size of interrogation windows ≈ 160 μm was chosen as a compromise between spatial resolution and robustness.

The displacement of the tissue between consecutive frames is evaluated on a square grid, with a spacing that is half the interrogation window size, bounded by a polygonal contour representing the border of the tissue. The border is identified in the first frame using an active contour or "snake"(*24*), and propagated to subsequent frames using the outcome of the PIV. Bilinear interpolation within the grid cells defines a continuous displacement field $d\mathbf{r}(\mathbf{r},t_i,t_{i+1})$, a velocity field

$$\mathbf{v}(\mathbf{r},t_i)=\frac{d\mathbf{r}(\mathbf{r},t_i,t_{i+1})}{t_{i+1}-t_i} \tag{S5}$$

and a mapping

$$M(\mathbf{r},t_i,t_{i+1})=\mathbf{r}+d\mathbf{r}(\mathbf{r},t_i,t_{i+1}) \tag{S6}$$

that can be extended to any pair of times by composition and linear interpolation between frames. In these terms, the trajectory of a point that occupied a position $\mathbf{r}_0$ at time t_0 is

$$\mathbf{r}(t)=M(\mathbf{r}_0,t_0,t) \tag{S7}$$

In most experiments, a small fraction of the tissue near the border eventually left the image frame (e.g. Fig. 1D). To reconstruct the motion of the full tissue, as required to measure the area of embryonic territories, and to register movies in space, points outside the image were assigned the velocity of the closest point along the image border. This extrapolation concerns only a small fraction of the tissue, and should closely approximate the true motion of the tissue, since motion near the tissue border is relatively uniform (e.g. Fig. 1B).

S2. Decomposition into divergent and rotational components

The decomposition of the velocity field shown in Fig. 1I, J is a variation on the Helmholtz-Hodge decomposition of a vector field into a divergent, irrotational component, and a rotational, divergence-free component (*31*). For our purposes (see Section S7 below), it is desirable to include the motion of the tissue border into the divergent component. Because the tissue can exhibit a net rotation (a non-zero circulation) along its border, this implies that the divergent component of the flow cannot be exactly irrotational. However, with a relatively uniform, outward motion of the border, it can be kept approximately irrotational.

To construct a divergent component that satisfies the above requirements, we first compute an unbounded, irrotational vector field $\mathbf{v}_i$ that has the same divergence as the tissue velocity **v**,

$$\nabla\cdot\mathbf{v}_i=\nabla\cdot\mathbf{v} \tag{S8}$$

This is equivalent to the Helmoltz decomposition of an unbounded vector field, which can be computed using a suitable Green's function. Numerically, with the displacements defined on a

square grid, we define an elementary displacement field (a Green's function) associated with the expansion of a single grid cell, and convolve it with the area changes of all the grid cells. Second, a divergence-free vector field $\mathbf{v}_b$ is added to match the motion of the tissue border. Anticipating on a fluid-mechanical description, this is obtained as the motion induced in an unbounded, incompressible fluid by tractions along the tissue border. Numerically, the tractions are taken to be uniform along the edges of a polygonal contour, and chosen to best match the displacement of the border in a least-squares sense.

Formally, the decomposition of the displacement field $d\mathbf{r}$ into divergent and rotational components $d\mathbf{r}_1$ and $d\mathbf{r}_2$ can be written as

$$d\mathbf{r}_1 \circ d\mathbf{r}_1\left(\left\{dA(c)\right\}, d\mathbf{r}_{|B}\right) = d\mathbf{r}_i\left(\left\{dA(c)\right\}\right) + d\mathbf{r}_b\left(d\mathbf{r}_{|B} - d\mathbf{r}_{i|B}\right) \tag{S9}$$

$$d\mathbf{r}_2 = d\mathbf{r} - d\mathbf{r}_1 \tag{S10}$$

where the $\left\{dA(c)\right\}$ denote the area changes of the grid cells, and $d\mathbf{r}_{|B}$ the displacement of the tissue border *B*.

S3. Identification of tissue regions

In our analysis, the embryo is described as two partially overlapping regions, an approximately circular region (referred to as *embryo proper* in this study) that is delimited by the *embryo margin*, and the *prospective primitive streak*. The margin has a finite width, representing an initially fuzzy boundary between embryonic and extra-embryonic tissue. The prospective primitive streak initially occupies a crescent-shaped region along the margin, that later converges and extends to give rise to the streak proper. At that stage, the embryo is thus idealized as an approximately circular region plus the elongated streak. In reality, the margin connects smoothly with the streak, as tissue converging towards the streak extends in the A/P direction. The margin, represented by a discrete *embryo contour*, the prospective primitive streak, and the orientation of the A/P axis are identified from the movement of the tissue, as follows.

S3.1. Embryo proper

The embryo margin is identified using an active contour or "snake" (*24*), based on the inhomogeneous deformations that make a morphological border evident in Fig. 1D. As a first step, we construct a function of space that changes sign at the margin. This combines two criteria to locate the border along the sides and in the anterior of the embryo.

Along the sides of the embryo, a border is seen because tissue on either side of the border is sheared in opposite directions, such that an initially straight line develops a kink (Fig. S1A-C). To assign a point **r** to one side, based on motion between times *t* and *t'*, we track the orientation of an initially radial segment centered on **r** (Fig. S1B, C; the segment initially points away from the putative center of the embryo, i.e. the center of the snake). Let $\mathbf{r} \pm \Delta\mathbf{r}/2$ denote the ends of the segment, and $\Delta\mathbf{r}'$ their separation at time *t*'. The vector difference

$$d\mathbf{o}(\mathbf{r},t,t') = \frac{\Delta\mathbf{r}'}{|\Delta\mathbf{r}'|} - \mathbf{e}_r' \tag{S11}$$

where $\mathbf{e}_r'$ is a unit vector pointing away from the embryo center at t', measures the change in orientation of the segment relative to the radial direction. The scalar

$$s_1(\mathbf{r},t,t') = \mathbf{a} \times d\mathbf{o}(\mathbf{r},t,t') \tag{S12}$$

where $\mathbf{a}$ is an anterior-oriented unit vector, is negative if the segment rotates faster than it moves about the embryo center, as is the case inside the embryo, and positive outside (Fig. S1C). In the anterior of the embryo, a border is apparent because of differential tissue expansion (Fig. 1D). Because the tangential deformation is continuous across the embryo border, it is mostly the radial deformation that varies across the border: the embryonic tissue contracts, while the extraembryonic tissue expands, in the radial direction (Fig. S1A-C). Tracking the orientation of an initially radial segment centered on **r** as before, the scalar

$$s_2(\mathbf{r},t,t') = \frac{\Delta\mathbf{r}'\cdot\mathbf{e}_r}{|\Delta\mathbf{r}|} - 1 \qquad \text{(S13)}$$

should thus be negative inside the embryo and positive outside (Fig. S1C).
A criterion to assign a point within the tissue, with a trajectory $\mathbf{r}(t)$, to embryo proper or extraembryonic tissue is obtained by combining the above criteria, s_1 and s_2, and integrating over time

$$s\{\mathbf{r}(t)\} = \sum_i \left\{ s_1\left[\mathbf{r}(t_i),t_i,t_{i+1}\right] + 2w_2\left[\mathbf{r}(t_i),t_i\right] s_2\left[\mathbf{r}(t_i),t_i,t_{i+1}\right] \right\} \qquad \text{(S14)}$$

In this equation, the weight

$$w_2 = \max(\mathbf{a}\times\mathbf{e}_r, 0) \qquad \text{(S15)}$$

where **a** and $\mathbf{e}_r$ denote anterior and radial unit vectors as before, is zero in the posterior and tends to 1 in the anterior, where the criterion s_2 is relevant; the prefactor of 2 is chosen to balance the two criteria, such that *s* is relatively uniform within the embryo (in the anterior vs. on the sides; Fig. S1D).
The function *s* defined above is used to fit a snake to the embryo margin. As a result of convergence towards the streak, an initially smooth contour can map to an irregular one in the final configuration of the tissue. To avoid this, the snake is parameterized by its final position. The "external force" used to evolve the snake, $\mathbf{f} = -s\mathbf{e}_r$, where $\mathbf{e}_r$ is evaluated in the final configuration, points outward inside the embryo and inward outside the embryo. To ensure that the initial configuration of the snake is also smooth, its internal energy is obtained by computing the internal energy from (*24*), which penalizes bending and stretching, in the initial and final configurations of the snake and taking the sum. As in (*24*), the snake is evolved using a stepping method that is explicit with respect to external forces and implicit with respect to internal forces.

S3.2. A-P axis

The orientation of the A-P axis is identified according to the motion of points along the embryo contour, which converge to the posterior (Fig. 1E-G). Let $\Theta(\theta,t,t')$ denote the angular position at time *t*' of a contour point that occupied position θ at time *t*. The angular displacement between times 0 and *t*, $d\theta(t) = \Theta(\theta,0,t) - \theta$, plotted as a function of θ, has a characteristic, approximately triangular shape (Fig. S1E). It exhibits two zero crossings, in the anterior and posterior of the embryo. The posterior of the embryo, used as a reference to define angular positions, is identified as the zero crossing with a negative slope (corresponding to angular contraction).
In the case of perturbation experiments where the axis rotates over time (Fig. 4H), this definition is adapted by subtracting the average angular displacement before identifying the zero crossings.

S3.3. Prospective primitive streak

The prospective primitive streak is identified according to the areal contraction of the tissue. With reference to the time of motion onset t_0 and the "streak stage" t_{95} (both defined in section S4 below), a portion of the tissue is considered to belong to the prospective primitive streak if its area decreases by more than 50% between the intermediate stage $t_m = (t_0 + t_{95})/2$ and t_{95}. Counting area changes from t_m rather than an earlier time point has little incidence on the definition, since aerial contraction is limited prior to t_m (Fig. 1H), and is convenient for the extraction of the streak contour by thresholding, since the prospective primitive streak has a compact shape at t_m (Fig. S1G). A finite threshold, 50% contraction, is required because some areas outside the streak also contract, albeit to a lesser extent. Mapping the streak contour forward and backward in time defines the location of the prospective primitive streak at arbitrary times (Fig. S1F, H).

We note that a broader region of the tissue will contribute to the late primitive streak, and will eventually form mesendodermal cells, as would be captured by evaluating the areal contraction of the tissue at a later stage. The above definition is intended to identify the tissue that contributes to the early streak. We note that areal contraction is initiated rather uniformly within that region (Fig. S4), supporting a distinction from the subsequent recruitment of adjacent tissue into the fully formed streak.

S4. Spatial and temporal registration

Embryos are registered in space using a common coordinate system (u,θ) that is derived from a polar coordinate system (r,θ) with its origin at the center of the embryo contour and $\theta = 0$ at the posterior (Fig. S1I). For each θ, the coordinate *u* is a piecewise linear function of *r*, interpolating from $u = 0$ at the origin, to $u = 1$ at the embryo contour, to $u = 2$ at the tissue border (these values are consistent with an average embryo radius ≈ 0.9 mm that is about half the average tissue radius ≈ 1.8 mm).

Embryos are registered in time according to the motion of points along the embryo contour. The angular extent $\alpha(t)$ of an initially 90º sector centered on the posterior is used to measure the progress of motion and define two temporal landmarks. First, the time t_0 of motion onset is defined by extrapolating backward from the time points t_{25} and t_{50} corresponding to 25% and 50% contraction of the sector, i.e. $t_0 = 2t_{25} - t_{50}$, with $\alpha(t_{25}) = 67.5º$ and $\alpha(t_{50}) = 45º$. Second, the time point t_{95}, corresponding to 95% contraction of the sector, i.e. $\alpha(t_{95}) = 4.5º$, was chosen as the typical time when a well-defined streak is visible.

The interval between t_0 and t_{95} is around 8 hours in control embryos (Fig. S1J). Thus, it is convenient to define a normalized time that interpolates linearly between 0 h at t_0 and 8 h at t_{95}. To adapt the above definition to treated embryos in which convergence to the posterior is delayed or comes to a halt, the times t_{25} and t_{50} are defined to correspond to 25% and 50% of the final contraction reached by the embryo, e.g. $\alpha(t_{50}) = (90 + \alpha_{final})/2$. In that case, the normalized time is defined relative to t_0, but without rescaling.

S5. Average embryo

With the embryos registered in space and time, it is possible to compute averages of any quantity of interest, and to construct an average embryo. To this end, the configuration of individual embryos at the time of motion onset is mapped to an average initial configuration, specified by an average tissue border and average embryo contour. Here, the average of a set of curves is defined as follows: the center of the average curve is the average of the curve centers; defining every curve in a polar coordinate system (r,θ) with the origin at its center, the average curve is obtained by averaging $r(\theta)$.

As a first step, the average displacement of a point in the average initial configuration is defined in the coordinate system (u,θ) introduced above as

$$\overline{\delta\mathbf{r}}(u,\theta,0,t) = \frac{1}{N}\sum_{i=1}^{N} \delta\mathbf{r}_i(u,\theta,0,t) \qquad \text{(S16)}$$

where *t* denotes normalized time (thus $t = 0$ is the time of motion onset). Averaging the displacement fields in this way is not guaranteed to preserve areas. As a corrective, we add at each time step a divergent displacement field, computed in the same way as the divergent component of the tissue flow (Section S2), such that area changes in the average embryo match the average area change across embryos.

S6. Apparent forces

For an incompressible viscous fluid that is described by the Stokes equation

$$\eta\Delta\mathbf{v} - \nabla P + \mathbf{f} = 0 \qquad \text{(S17)}$$

the negative of the Laplacian of the velocity field, $-\Delta\mathbf{v}$, is proportional to the forces driving motion, i.e. the pressure gradient $-\nabla P$ and the external force density **f**. For motion that is driven by active internal stresses, **f** should be replaced by the divergence $\nabla\cdot\sigma_a$ of the active stress tensor, which acts as an apparent external force.

Turning to tissue flows in the embryo, the Laplacian of the velocity field has contributions from the divergent and rotational components of the flow,

$$-\Delta\mathbf{v} = -\Delta\mathbf{v}_1 - \Delta\mathbf{v}_2 \qquad \text{(S18)}$$

Recalling that $\mathbf{v}_1$ is defined as an irrotational flow $\mathbf{v}_i$ with the same divergence as **v**, plus an incompressible flow $\mathbf{v}_b$ driven by border tractions (Section S2), we have

$$-\Delta\mathbf{v}_i = -\nabla(\nabla.\mathbf{v}_i) = -\nabla(\nabla.\mathbf{v}) \qquad \text{(S19)}$$

where the first identity results from $\mathbf{v}_i$ being irrotational, and

$$-\Delta\mathbf{v}_b = -\nabla P_b / \eta \qquad \text{(S20)}$$

inside the border, by definition of $\mathbf{v}_b$, thus

$$-\Delta\mathbf{v}_1 = -\nabla(\nabla.\mathbf{v}) - \nabla P_b / \eta \qquad \text{(S21)}$$

In other words, the driving forces associated with the divergent component of the flow arise from the pressure field P_b induced by the border tractions, and from the gradient of the divergence of **v**. The border tractions are typically a small correction, and the resulting pressure gradient, extending on the large scale of the tissue, makes a small contribution. As for the divergence, there are two contributions, associated with graded expansion of the extra-embryonic tissue, and

with localized areal contraction at the streak. From Fig. 1I, J, the sharpest gradient is along the streak. Taken together, the Laplacian of the velocity field (Fig. 2A) can be interpreted as the sum of three dominant contributions: an apparent external force driving tissue movement, corresponding to the divergence of active internal stresses (arrows along the embryo margin); the resulting pressure gradient (forward arrows inside the embryo proper); and areal contraction at the streak (inward arrows along the streak).

S7. Fluid-mechanical model

S7.1. Rationale

The model describes tissue flows in the embryo as the motion of a fluid, with three driving terms: (1) areal expansion or contraction of the tissue; (2) traction from border cells attached to the vitelline membrane; and (3) active stresses along the embryo margin. Although it is in some cases possible to treat areal expansion and contraction as simple responses to mechanical stress, by modeling the tissue as a compressible fluid (*9*), this would not explain well the area changes observed here. Indeed, the extraembryonic tissue expands much less near the border than away from it (Fig. 1C, D), when a compressible model would predict a relatively uniform expansion in the absence of active stresses in that region. Conversely, the non-uniform stresses driving movement within the embryo proper should result in non-uniform area changes, in contrast with the approximately area-preserving flow observed in that region (except for the primitive streak; Fig. 1C, D, H-J). Instead, areal expansion and contraction are treated here as intrinsic behaviors of the tissue, while mechanical stresses induce shearing alone. Biologically, this amounts to taking proliferation, cell area changes, and ingression as autonomous behaviors, tied to regional identity, while the response to mechanical stress is mostly in the form of cell rearrangements. Again, this is not meant to imply that these cellular behaviors are actually insensitive to mechanical stresses, but as a mathematical simplification. Since tissue area changes correlate with cell identity, their regulation, like the regulation of active stresses along the margin, may involve a complex interplay between mechanics, gene expression/cell fate, and cellular behaviors, all of which lies beyond the scope of the present study.

S7.2. Equations of motion

The above description amounts to a fluid-mechanical model of an effectively incompressible tissue, with area changes resulting from locally isotropic growth, for which equations of motion can be postulated without reference to the short-term, elastic response of the tissue (*32*). Here, with a view to the interpretation of ablation experiments that probe tissue stresses (see Section S8.2 below), we explicitly derive a fluid model as the long-time limit of a viscoelastic description, similar to (*9*) in the compressible case. Assuming Maxwell behavior, the tissue stress takes the form of a transient elastic stress $\boldsymbol{\sigma}_e$ that relaxes with a characteristic time t_r. For an effectively incompressible tissue, only the shear stress relaxes. Decomposing $\boldsymbol{\sigma}_e$ into the shear stress s_e and a pressure P,

$$\boldsymbol{\sigma}_e = s_e - P\mathbf{I} \tag{S22}$$

where **I** denotes the identity tensor, the elastic stress satisfies

$$\dot{\sigma}_e = \dot{s}_e - \dot{P}\mathbf{I} = S\left[\nabla\mathbf{v} + (\nabla\mathbf{v})^T - (\nabla\cdot\mathbf{v})\mathbf{I}\right] + B\frac{\nabla\cdot\mathbf{v} - \gamma}{2}\mathbf{I} - \frac{1}{\tau_r}s_e \tag{S23}$$

In the above equation, $\nabla\mathbf{v} + (\nabla\mathbf{v})^T - (\nabla\cdot\mathbf{v})\mathbf{I}$ is twice the shear rate tensor; γ is the local areal growth rate, thus $\nabla\cdot\mathbf{v} - \gamma$ is the rate of elastic expansion; and *S* and *B* are the shear and bulk moduli characterizing the elastic response of the tissue (although effectively incompressible on the long term, the tissue can expand or contract elastically).
In the limit of a near-steady-state flow, $\dot{\sigma}_e$ vanishes. Taking the isotropic part of equation (S23) yields

$$\nabla.\mathbf{v} = \gamma \tag{S24}$$

i.e. the divergence of the velocity coincides with the areal growth rate in the long-time limit. The anisotropic part yields

$$s_e = \tau_r S\left(\nabla\mathbf{v} + (\nabla\mathbf{v})^T - (\nabla\cdot\mathbf{v})\mathbf{I}\right) \tag{S25}$$

i.e. the tissue responds to shear as a fluid with an effective viscosity

$$\eta = \tau_r S \tag{S26}$$

Neglecting inertial terms, the tissue satisfies the force balance equation

$$\nabla\cdot\sigma_e + \mathbf{f} + \nabla\cdot\sigma_a = 0 \tag{S27}$$

where we have included both an external force density $\mathbf{f}$ and an active internal stress σ_a for greatest generality. Combining equations (S22) and (S24)-(S27), and using the identity $\nabla\cdot(\nabla\mathbf{v}) = \nabla(\nabla.\mathbf{v})$, we finally obtain the equations of motion

$$\rho D\mathbf{v} - \nabla P + \mathbf{f} + \nabla\cdot\sigma_a = 0 \tag{S28}$$

$$\nabla.\mathbf{v} = \gamma \tag{S29}$$

In other words, the long-term motion of the tissue is described by the Stokes equations of viscous flow, with an additional source term, in the form of a prescribed non-zero divergence. The viscous shear stress and pressure appearing in that description identify respectively with the anisotropic and isotropic components of the transient elastic stress.

S7.3. Source terms and boundary conditions

In applying the above model to the embryo, we assume that motion is driven by active internal stresses within the tissue, with external forces being restricted to the border cells attached to the vitelline membrane. The relatively uniform, outward motion of the tissue border (Fig. 1I, J) is treated as independent of the forces acting within the tissue. Thus, the boundary condition of the model is a fixed border velocity, and the border tractions do not explicitly appear as a source term. This motivates *a posteriori* our definition of the divergent and rotational components of the flow (Section S2). In the model, the divergent component coincides with the contribution of area changes and border motion, while the rotational component coincides with the contribution of active internal stresses.

S7.4. Eulerian and Lagrangian treatment of area changes

When fitting the model to an individual or an average embryo, the motion of the border and area changes are taken from experiment. The source term associated with area changes, γ in equation (S29), can be chosen in two ways. In a "Eulerian" treatment, it is chosen independently at each time step to match the divergence of the observed tissue velocity,

$$\gamma = \nabla\cdot\mathbf{v}_{\text{exp}} \tag{S30}$$

As a result, the divergent component of the velocity in the model is exactly the divergent component of the observed velocity,

$$\mathbf{v}_1 = \mathbf{v}_1^{\exp} \tag{S31}$$

With this choice, however, the model would exhibit areal contraction in the region of the primitive streak, even if it failed to account for the motion that forms the streak from an initially crescent-shaped region.

If we hold that area changes are tied to a regional identity that the tissue carries with itself in its motion, we should instead adopt a "Lagrangian" treatment of area changes, i.e. the areal growth rate is a property of material points moving with the tissue,

$$g\left[M(\mathbf{r},0,t) \right] = \left(\nabla . \mathbf{v}_{\exp} \right) \left[M_{\exp}(\mathbf{r},0,t) \right] \tag{S32}$$

where M and $M_{\exp}$ denote the mapping induced by the flow in model and experiment.

Numerically, the target area change $dA(c)$ of a grid cell c between two consecutive time points, t_i and t_{i+1}, is computed by tracking back the location of the cell from t_i to the initial configuration under the model mapping then forward to t_{i+1} under the experimental mapping,

$$\delta A(c) = A\left[M\left(\tilde{M}\left(c, t_i, 0 \right), 0, t_{i+1} \right) \right] - A(c) \tag{S33}$$

The resulting displacement field, with an unchanged boundary condition, is computed in the same way as the divergent component of the flow (Section S2).

S7.5. Active stresses

Rotational motion in the model is driven by active tensile stresses along the embryo margin, which is described by a contour $C(t)$ and a width w. The margin is assumed to be advected with the flow, thus in simulations the contour $C(t)$ is updated at each time step, whereas the width w is taken to be constant. The active stress is oriented tangentially, with a Gaussian profile across the margin,

$$s_a(\mathbf{r},t) = \frac{T(q,t)}{\sqrt{2pw^2}} e^{-\frac{d^2}{2w^2}} \mathbf{e}_t \ddot{A} \mathbf{e}_t \tag{S34}$$

In this equation, $T(q,t)$ is the tension profile as a function of the angle q relative to posterior, d is the distance between $\mathbf{r}$ and the embryo contour, and $\mathbf{e}_t$ is a unit vector tangent to the contour. The factor $\sqrt{2pw^2}$ in the denominator ensures that the stress integrated across the margin equals the tension $T(q,t)$. Because the tissue is treated as effectively incompressible, the isotropic component of the active stress induces no motion, and the choice of a uniaxial stress, adopted here, is not restrictive.

At each time step, the motion induced by active stresses is computed according to the current location of the embryo margin and tension profile. Numerically, we first solve for the motion driven by the active stress in a box with periodic boundary conditions, in Fourier space, then add border tractions to satisfy the boundary condition, as for the decomposition of the displacement field (Section S2).

S7.6. Model fitting

To fit the model to the observed tissue flow, the initial position $C(0)$ of the embryo contour is represented by a truncated Fourier series in polar coordinates, with a center point (r_1, r_2) and a radius

$$r(\theta) = r_0 + \sum_{k=2}^{n_r} r_{2k-1}\cos k\theta + r_{2k}\sin k\theta \qquad \text{(S35)}$$

where the series includes no $k = 1$ modes because they are redundant with translation of the center point. Similarly, the tension profile at each step is described as

$$T(\theta, t_i) = T_0(t_i) + \sum_{k=1}^{n_T} T_{2k-1}(t_i)\cos k\theta + T_{2k}(t_i)\sin k\theta \qquad \text{(S36)}$$

A uniform tension along a circular contour induces no motion, and the average tension along the approximately circular embryo contour cannot be estimated reliably. As a convention, the average tension T_0 is chosen such that the tension vanishes in the anterior, i.e. $T(\pi) = 0$.

Given an initial position $C(0)$ and width *w* of the contour, the coefficients $T_k(t_i)$ are fit iteratively. At each time step, they are chosen to minimize the residual

$$R_i^2 = \sum_{\mathbf{r}} \left| \delta\mathbf{r}_{\exp}(\mathbf{r}, t_i, t_{i+1}) - \delta\mathbf{r}(\mathbf{r}, t_i, t_{i+1}) \right|^2 \qquad \text{(S37)}$$

where the sum is over the grid vertices, a linear least squares problem. Then, the position of the contour is updated according to the model flow, $C(t_{i+1}) = M\left(C(t_i), t_i, t_{i+1}\right)$. And so on.

This leaves the parameters $\{r_k\}$ of the initial contour position, and the width *w*, as free parameters of the model. These are fit by minimizing the global residual

$$R^2 = \sum_i R_i^2 \qquad \text{(S38)}$$

using the Levenberg-Marquardt algorithm (*33*). In practice, most embryos are close enough to circular that initializing the model with a circular contour yields a good fit, that is only marginally improved by allowing for more general shapes ($n_r \geq 2$). The embryo contour obtained in this way agrees well with the location of the embryo margin derived from the deformations of the tissue (to within a few percent of the radius for the average reference embryo). As for the tensions, $n_T = 4$ was chosen as a compromise between minimizing the residual and avoiding overfitting. Larger values of n_T yield no significant improvement in the fit, but noisier tension profiles.

Because model fitting requires repeated simulations, the Lagrangian treatment of area changes (Section S7.4) would be prohibitive, thus the Eulerian treatment is used. *A posteriori*, a Lagrangian simulation is run with the same initial contour position and width, but estimating the tensions anew, to evaluate the residual under that formulation. Consistent with the fact that the model explains well the rotational movement of the tissue, the residual in the Lagrangian formulation is only marginally larger than in the Eulerian formulation, e.g. 9.5% vs. 9.3% for the average embryo (normalized step-by-step residuals as defined in Materials and Methods).

S7.7. Synthetic embryo

The "synthetic embryo" of Fig. S3 was derived from a fit of the model to a symmetrized, average embryo, obtained by including a mirror image of each embryo in the averaging procedure of Section S5. The two modes representing area changes in Fig. 2H are simplified from a more detailed description (Fig. S4), with separate terms for:

(1) uniform expansion within the embryo proper;

(2) an A-P gradient in expansion within the embryo, that captures early areal contraction in the posterior of the embryo;

(3) expansion of the extra-embryonic tissue;
(4) reduced expansion near the tissue border;
(5) areal contraction of the prospective primitive streak.
The log of the relative area of a portion of tissue at position **r** (in the initial configuration of the average embryo) is modeled as a linear combination of these five modes:

$$\log a(\mathbf{r},t) = \sum_{i=1}^{5} a_i(t) m_i(\mathbf{r}) \tag{S39}$$

For all but the border mode m_4, position is defined in a coordinate system (u,θ) that is derived from a polar coordinate system (r,θ) with its origin at the center of the embryo contour, taken from the model fit, and $\theta = 0$ at the posterior. If $r_c(\theta)$ is the polar representation of the embryo contour, we set $u = r / r_c(\theta)$ such that $u = 1$ along the contour.
The transition from embryo proper to extra-embryonic tissue is represented by a sigmoidal function

$$e(u) = \frac{1 - \tanh(2(u - u_e)/w_e)}{2} \tag{S40}$$

that steps from 1 to 0 around $u = u_e$, with a width w_e. In these terms, the modes corresponding to uniform expansion of the embryo, graded expansion within the embryo, and expansion of the extra-embryonic tissue, are defined by

$$\begin{aligned} m_1(u,\theta) &= e(u) \\ m_2(u,\theta) &= -e(u)u\cos\theta \\ m_3(u,\theta) &= 1 - e(u) \end{aligned} \tag{S41}$$

The border term is expressed in a different coordinate system, (d,θ), where *d* is the distance to the tissue border

$$m_4(d,\theta) = -e^{-\frac{d^2}{2w_b^2}} \tag{S42}$$

and taken to decay as a Gaussian away from the border, with a width w_b.
Finally, areal contraction at the streak is described by a Gaussian function of *u* and θ

$$m_5(u,\theta) = -e^{-\frac{(u-u_s)^2}{2w_s^2} - \frac{\theta^2}{2\Theta_s^2}} \tag{S43}$$

with parameters u_s, w_s, and Θ_s for the position, width, and angular extent of the prospective primitive streak (in its initial, crescent-shaped configuration). The synthetic embryo of Fig. S3 was obtained by grouping the modes corresponding to uniform expansion of the embryo, to the extra-embryonic tissue, and to the tissue border (m_1, m_1, and m_4), and approximating their temporal evolution by a straight line. The gradual onset of areal contraction at the streak (m_5) is approximated by a smooth curve with a slope that steps from zero to a finite value as a sigmoid:

$$a_5'(t) \propto \frac{1 + \tanh\frac{2(t - t_s)}{t_s}}{2} \tag{S44}$$

with parameters t_s and t_s for the time and rate of the onset (Fig. S3A). The A-P gradient within the embryo (m_2), which is limited in amplitude and transient, is omitted. Its inclusion in the detailed model is nevertheless useful to distinguish between contraction along the streak and initial contraction in the posterior of the embryo.

While the areas changes are expressed relative to the *initial* configuration of the tissue, the active stresses along the margin are taken to maintain a constant angular dependence in the *current* configuration of the tissue, with a Gaussian profile and a time-dependent amplitude that combines a sigmoidal step for the onset of motion and an exponential for the decrease in tension at later times

$$T(q,t) = T_{\max} \frac{1 + \tanh \frac{2(t - t_T)}{t_T^+}}{2} e^{-\frac{t}{t_T^-} - \frac{q^2}{2\Theta_T}} \tag{S45}$$

with parameters $T_{\max}$ for the maximum tension, Θ_T for the angular extent of the tension gradient, t_T^+ and t_T^+ for the time and rate of onset, and t^- for the decay (Fig. S3A). The width of the Gaussian is obtained from a fit to the time-averaged tension profile of the main model (itself fit to experimental data), and the parameters of the time-dependent amplitude from a fit to the tension in the posterior in the main model, i.e. $T(0,t)$ in equation (S36). As initial and boundary conditions, the synthetic embryo has a circular, initial contour, taken from the model fit, and the tissue is assumed to maintain a circular border over time, with the same initial center and area as the average embryo.

This fully specifies a "synthetic embryo" that is defined only from analytical functions. Since area changes are specified relative to the initial configuration of the tissue, it is simulated using the "Lagrangian" treatment of areas (Section S7.4). Fig. S3 and Movie S6 were generated with the parameter values in Table S1.

S7.8. Analytical model

The motion induced by active stresses can be computed analytically in the limit of a vanishing margin width, if the embryo contour and tissue border are circular and concentric. In that limit, the tension profile $T(q)$ maps to an external force density

$$\mathbf{F}(q) = \frac{T'(q)}{r_c}\mathbf{e}_q - \frac{T}{r_c}\mathbf{e}_r \tag{S46}$$

along the embryo contour, with radius r_c. In the following, we consider a sinusoidal tension profile, with a differential ΔT between anterior and posterior,

$$T(q) = \frac{\Delta T}{2}\cos q \tag{S47}$$

or in complex notation

$$T(q) = \frac{\Delta T}{2} e^{iq} \tag{S48}$$

The calculation readily generalizes to higher-order Fourier modes, thus to any tension profile that is expressed as a Fourier series. The velocity field is derived from the stream function ψ, which satisfies the biharmonic equation $\Delta^2 \psi = 0$, with solutions of the form

$$\psi(r,q) = \phi(r) e^{iq} \tag{S49}$$

The equation is solved in the embryo and in the extraembryonic tissue, then the solutions are matched at the margin, by relating the stress jump across the border to the force density

$$\boldsymbol{\sigma}_{out}\cdot\mathbf{e}_r - \boldsymbol{\sigma}_{\text{int}}\cdot\mathbf{e}_r + \mathbf{F} = 0 \tag{S50}$$

This straightforward calculation yields the velocity field

$$v_r = \frac{\Delta T}{16\mu}\frac{r_b^2 - r_c^2}{r_b^4 r_c^2}\left[(r_b^2 + r_c^2)r^2 - 2r_b^2 r_c^2\right]\cos\theta \tag{S51}$$

$$v_\theta = \frac{\Delta T}{16\mu}\frac{r_b^2 - r_c^2}{r_b^4 r_c^2}\left[2r_b^2 r_c^2 - 3(r_b^2 + r_c^2)r^2\right]\sin\theta \tag{S52}$$

inside the embryo ($r < r_c$) and

$$v_r = -\frac{\Delta T}{16\mu}\frac{r_c^2}{r_b^4 r^2}(r_b^2 - r^2)^2\cos\theta \tag{S53}$$

$$v_\theta = -\frac{\Delta T}{16\mu}\frac{r_c^2}{r_b^4 r^2}(r_b^2 - r^2)(r_b^2 + 3r^2)\sin\theta \tag{S54}$$

outside the embryo ($r > r_c$), with r_b the border radius (Fig. S5).

The "swimming speed" of the embryo is obtained as the average velocity inside the embryo, projected along the anterior direction,

$$v_e = \frac{\Delta T}{16\mu}\left(1 - \frac{r_c^2}{r_b^2}\right)^2 \tag{S55}$$

In a moving frame that follows the embryo, the velocity at the embryo contour is tangential, thus a circular embryo would maintain a stationary shape in an unbounded medium. The tangential velocity at the contour, which fully determines deformations inside the embryo, is

$$v_\theta = -\frac{\Delta T}{8\mu}\left[1 - \left(\frac{r_c}{r_b}\right)^4\right]\sin\theta \tag{S56}$$

Comparing equations (S55) and (S56), the progress of motion inside the embryo is less sensitive to the presence of the border than the swimming velocity, approaching its asymptote more rapidly as r_b / r_c increases (Fig. S5D). With a border radius that is just 50% larger than the embryo radius, the velocity along the embryo contour is above 80% of its limiting value.

S7.9. Sensitivity analysis

Here, we present a brief sensitivity analysis of the model, focusing on the parameters that control the pattern of active stresses. The table below shows how the output of the synthetic model varies with each of these parameters. Changes in parameter values are measured relative to their default values from Table S1 (or to the initial radius of the embryo contour in the case of changes in its initial position), and the effect of the output is measured by the change in the final displacement field $\delta\mathbf{r}(t_1, t_n)$, normalized by the magnitude of the displacements with the parameter set of Table S1 (similar to our definition of the normalized end-to-end model residual, Eq. S4). For instance, the sensitivity of 1.8 for the parameter r_c means that a 1% increase in the initial radius of the embryo contour results in a 1.8% change in the output of the model. The synthetic model is used here because it has fewer parameters, and because the patterns of active

stress and area change vary in consistent ways when the initial position of the embryo contour is modified.

parameter		sensitivity
x_c	initial position of the embryo contour along the left-right axis	$\frac{r_c}{\lvert d\mathbf{r}\rvert}\left\lvert\frac{\partial}{\partial x_c} d\mathbf{r}\right\rvert \approx 2.3$
y_c	initial position of the embryo contour along the A-P axis	$\frac{r_c}{\lvert d\mathbf{r}\rvert}\left\lvert\frac{\partial}{\partial y_c} d\mathbf{r}\right\rvert \approx 2.0$
r_c	initial radius of the embryo contour (here, EE expansion is adjusted to maintain the same final tissue area)	$\frac{r_c}{\lvert d\mathbf{r}\rvert}\left\lvert\frac{\partial}{\partial r_c} d\mathbf{r}\right\rvert \approx 1.8$
w	margin width	$\frac{w}{\lvert d\mathbf{r}\rvert}\left\lvert\frac{\partial}{\partial w} d\mathbf{r}\right\rvert \approx 0.05$
Ω_T	angular extent of the tension gradient	$\frac{\Omega_T}{\lvert d\mathbf{r}\rvert}\left\lvert\frac{\partial}{\partial \Omega_T} d\mathbf{r}\right\rvert \approx 0.4$
T	peak tension	$\frac{T}{\lvert d\mathbf{r}\rvert}\left\lvert\frac{\partial}{\partial T} d\mathbf{r}\right\rvert \approx 0.6$

Initial embryo contour position and radius

This analysis shows that the outcome of the model is very sensitive to the initial position and radius of the embryo contour. Shifting the embryo contour in either direction by just 50μm (while leaving the other parameters unchanged), or increasing its radius by the same amount (adjusting here the parameter for EE expansion to maintain the same final radius of the epiblast), is enough to displace the outcome of the model by more than 10%, in excess of the residual of our main model. This is not surprising, since the position of the embryo contour governs the global pattern of motion.

Amplitude and angular extent of the tension gradient

Similarly, the model is sensitive to changes in the amplitude and angular extent of the tension gradient along the margin, which govern the amplitude and the angular pattern of motion (as represented in Fig. 1G).

Margin width

On the other hand, the model is much less sensitive to changes in the width of the margin (by about an order of magnitude). This is seen in the table above, which describes the effect of small parameter changes in the synthetic model. Considering instead larger changes, applied in our main model, we find that setting the margin width to 0.25mm, corresponding to about double its default value, and fitting the other parameters to our average embryo, only increases the residual to 11.4% (instead of 9.4% for our main fit). This is, again, not surprising if the global displacement field is used as a measure, since the width of the margin affects motion mostly at the margin, determining the sharpness of the transition in velocity and deformation patterns across the margin (cf. Fig. S5C, which compares motion induced by margins of finite and

vanishing width). Indeed, the location of the margin and profile of active tension (active stress integrated across the margin) are the essential features that govern large-scale motion (which explains our choice of parameterization).
Taken together, our global fit may appear to not strongly constrain the margin width. On the other hand, the sharpness of the transition at the margin is predicted to be a direct readout of the width of the region where active stresses are generated. By this measure, velocity profiles across the margin of our average embryo would suggest that this region cannot be much larger than the margin width derived from our fit (Fig. S6).

S8. Analysis of laser ablation experiments

S8.1. Quantification of tissue strain

The response to laser cuts is analyzed using PIV, in the same way as for the analysis of tissue flows, with smaller interrogation windows ≈ 40 μm to achieve higher spatial resolution, and without prior filtering. The response of the tissue inside and outside the cut is quantified according to the motion of initially circular contours on either side of the cut, with radii 2/3 and 4/3 of the cut radius. The tissue strain is measured from the displacement of these contours after an interval of 2 minutes, chosen such that elastic stresses are close to fully relaxed, but subsequent tissue flow (on the scale of the hour) can be neglected. The deformation of each contour is measured by the linear transform **F** that best fits its displacement, a mesoscopic analog of the deformation gradient of large deformation theory. In terms of **F**, radial and tangential stretch ratios can be defined as $\lambda_r = 1/|\mathbf{Fe}_r|$ and $\lambda_q = 1/|\mathbf{Fe}_q|$ for the inner contour, and as $\lambda_r = |\mathbf{Fe}_r|$ and $\lambda_q = |\mathbf{Fe}_q|$ for the outer contour, which relaxes in the opposite direction. The tangential vs. radial strain anisotropy plotted in Fig. 3C is defined as $\log(\lambda_q / \lambda_r)$. The inner and outer contours yield consistent values of the strain anisotropy; because tracking of the larger outer contour is more robust, the corresponding value is used to measure the response.

S8.2. Interpretation

The viscous stress in the fluid description identifies in a viscoelastic description with a transient elastic shear stress (Section S7.2). In that description, the tissue stress is the sum of the elastic stress and active stress,

$$\sigma = \sigma_e + \sigma_a \tag{S57}$$

The cut releases the tissue stress without (initially at least) affecting the active stress. Thus, it probes the elastic deformation of a portion of tissue relative to the configuration it would adopt under the effect of active stress alone, with a free border.
Based on the model, the viscous stress, thus the transient elastic shear stress, should be of the order of $\Delta T / r_e$, where ΔT is the tension differential between posterior and anterior, and r_e is the radius of the embryo. The active stress is of the order of $\Delta T / w$, where w is the width of the contractile embryo margin. Because the width of the margin is a fraction of the embryo radius, we expect the active stress to be the dominant contribution along the margin, whereas ablations inside the embryo probe the viscous stress (strains ≈ 2.5% inside the embryo, compared to strain rates ≈ 20%/h in the region of the cuts, can be used to estimate a relaxation time of the order of 10 min).
The tissue strain revealed by ablations is obviously an indirect measure of tissue stress. Nonlinear and anisotropic material properties may complicate the relation between stress

anisotropy and strain anisotropy, especially along the embryo margin, where deformations are largest and cells are elongated. However, because the largest deformations are in the tangential direction, and there is a greater density of junctions in that direction, we expect that the measured strain anisotropy, if anything, underestimates the underlying stress anisotropy.

S8.3. Comparison with stress patterns in the model

Since the average tension along the margin has little effect on motion in the model (exactly no effect for a perfectly circular margin), and cannot be reliably estimated from the observed motion, we have assumed a vanishing tension in the anterior as a default. *A posteriori*, our laser ablation experiments indicate that tension is present also in the anterior. Although this has no incidence on our description of tissue motion, we must allow for tension in the anterior if we want to compare the pattern of tissue stresses in the model with the experimentally observed tissue strains. A simple choice is to set the average tension at each time point such that the tensions in the anterior and posterior are in a fixed ratio. Fitting the model to our average embryo with the anterior tension set to a third of the posterior tension has almost no effect on the quality of the fit (yielding a residual of 9.8% instead of 9.4%). This modified model, at the intermediate time t=4 h, predicts a shear stress (integrating its active and passive components) that is about half as large in the anterior margin as in the posterior margin (at 45º from the posterior, corresponding to the location of the cut), and under a tenth as large inside the EP (midway between the center of the EP and the anterior margin, corresponding to the location of the cuts). That is, the predicted differences in tissue stress are qualitatively consistent with but larger than the observed differences in tissue strain. We note, however, that the predicted differences depend on the width of the margin in the model (for a given tension profile, the active stress varies inversely with the margin width), and that our best fit for the margin width is in the lower range of the widths determined from the analysis of fixed embryos. With a wider margin, stresses inside the EP may also receive a small contribution from active stresses. If we fit our model with the margin width set to 0.17 mm instead of 0.12 mm, and the same ratio between tensions in the anterior and posterior, this only marginally increases the residual (to 10.3%), and predicts stress ratios ≈ 0.56 between anterior and posterior margin, and ≈ 0.14 between EP and posterior margin, which are closer to agreeing with the experimentally measured differences in tissue strain, to within the uncertainty in these measurements.

S8.4. Linear cuts

As described above, we have used circular laser cuts, and the resulting estimate of tissue strains, to characterize the mechanical state of the epiblast. The initial opening velocity of these cuts, which could provide a more direct measure of tissue stress (*8*), could not be determined, since relaxation was fast compared to the time to make the cut (~ 30s), and since several passes were sometimes needed to fully cut the tissue, as required for a reliable estimate of the tissue strain (the laser was thus run continuously and the opening measured after 2 min). To compare the initial opening velocity and final opening upon cutting, and check that they provide consistent estimates of the mechanical state of the tissue, we performed faster, linear cuts (in a radial direction, thus probing the orthoradial stress/strain). Although we cannot be certain that the tissue is fully cut in that case, this is inessential for the comparison between initial opening velocity and final opening.

To analyze the response to linear cuts, we tracked, using PIV as for the circular cuts, the relative motion of points on either side of the cut, at different distances from the cut (25μm, to track the motion of the cut edges while allowing for the width of the cut; and 100, 200, and 400μm, to track the propagation of motion away from the cut).

To interpret the response, we must depart from the material description adopted to model the long-term motion of the tissue. To derive a fluid-mechanical model, we idealized the tissue as a Maxwell material that dissipates elastic stress through cell rearrangements and deforms at a constant rate under constant applied shear stress (cf. section S7.2); in this description, the tissue opens instantaneously following a cut. On the short time scale of relaxation following a cut (seconds), stress dissipation through cell rearrangements (on a time scale ~ 10min, cf. section S8.2) can be neglected, and we must instead allow for the sources of dissipation that resist the opening, i.e. the internal viscosity of the tissue (resistance to cell deformations) and/or external friction. In this regime, the tissue can be idealized as a Kelvin-Voigt material, which relaxes to a finite, reversible elastic deformation under constant applied stress. If external friction is important, the response should gradually diffuse away from the cut (*8*). But we observe instead simultaneous motion at different distances from the cut (Fig. S7B, C), with a time course that is well captured by an exponential, arguing against a role for external friction (*a fortiori*, it is thus safe to ignore friction on the time scale of morphogenetic movements). Using the initial slope and asymptote of the exponential to measure the initial opening velocity and final opening of the cut, we find that the two are strongly correlated (Fig. S7A; Pearson correlation coefficient r=0.78; equivalently, we find a uniform relaxation time of 2.2 ± 0.8 s), suggesting that they provide consistent estimates of the mechanical state of the tissue. Indeed, measurements at different positions in the epiblast show the same trends as estimates of strain anisotropy from circular cuts, albeit with a greater dispersion, which may result from the tissue not always being fully cut and/or from variability in the isotropic part of the tissue stress, which also contributes to the opening of linear cuts.
Taken together, these experiments validate our use of the tissue strain to probe the mechanical state of the epiblast. Justifying our choice of circular cuts, we note that obtaining a reliable estimate of the stress or strain anisotropy - which is of interest here - from linear cuts would take many more experiments, since the stress or strain in different directions is measured in different embryos, whereas each circular cut provides a direct estimate of strain anisotropy. In addition, these experiments validate our choice of neglecting external friction in describing morphogenetic movements in the epiblast.

S9. Analysis of fixed embryos

For the analysis of fixed embryos, the apical signal was first extracted by fitting a smooth surface to the apical surface of the tissue, based on the ZO-1 channel. The signal for each channel (ZO-1 and myosin) was taken from a 1 μm slice along the surface.

S9.1. Quantification of cell shapes

Cells were segmented as described in Methods, based on the ZO-1 channel. The resulting binary image was used to define a polygonal boundary for each cell, connecting its border pixels. Cell shape anisotropy was measured by fitting an ellipse to each cell. With the ellipse represented by a matrix E (the linear transform that maps a unit circle onto an ellipse with the same inertia tensor as the cell), expressed in polar coordinates, the elements E_{qq} and E_{rr} measure the elongation of the cell along the tangential and radial directions, and the tangential vs. radial anisotropy of the cell (cell shape anisotropy) displayed in Fig. 3F, I, L, O and Figs. S8-S13, and S18, is defined as the dimensionless number $\log(E_{qq} / E_{rr})$.

S9.2. Quantification of myosin anisotropy

For the analysis of myosin anisotropy, a mask $z(i,j)$ is first generated from the ZO-1 channel to isolate the junctional myosin signal. To correct for variations in ZO-1 intensity, the intensity of each pixel is normalized by a measure of the local ZO-1 density along junctions, obtained as the ratio between the local density of ZO-1 signal (per unit area) and the local density of junctions (junction length per unit area). The former is obtained by smoothing the ZO-1 channel with a Gaussian filter, with a width of 50 μm » 5-10 cell diameters. The latter, by creating an image where each edge from the segmentation is replaced by a pixel with an intensity equal to its length, and convolving with the same Gaussian filter. The junctional myosin signal $m_j(i,j)$ is defined as the product of the original myosin signal $m(i,j)$ by the mask

$$m_j(i,j) = z(i,j)m(i,j) \tag{S58}$$

An orientation is then assigned to the junctional myosin by defining a local orientation tensor. This is constructed from the segmented image, as follows. First, each foreground pixel (i,j) in the segmented image is assigned an orientation $\mathbf{o}_f(i,j) = \mathbf{e} \ddot{A} \mathbf{e}$, where **e** is a unit vector parallel to the junction to which the pixel belongs (parallel to a line connecting the endpoints of the junction). An orientation $\mathbf{o}(i,j)$ is then defined across the image by smoothing the foreground orientation $\mathbf{o}_f(i,j)$ with a Gaussian filter to produce a smoothed orientation $\mathbf{o}_s(i,j)$, then computing

$$\mathbf{o}(i,j) = \frac{\mathbf{o}_s(i,j)}{c + \left|\mathbf{o}_s(i,j)\right|} \tag{S59}$$

With a standard deviation of the filter of one pixel, and a small value $c = 10^{-3}$ in equation (S59), the norm of the orientation **o** is close to 1 near junctions but decays rapidly a few pixels away from junctions, i.e. an orientation is defined only close to junctions.

Expressing the orientation tensor $\mathbf{o}(i,j)$in polar coordinates, the scalar $o_{qq}(i,j) - o_{rr}(i,j)$ is a measure of tangential vs. radial orientation that is used to color-code junctional myosin orientation (by interpolating between green and magenta for the extreme values 1 and -1) in Fig. 3G, M, Fig. 4D and Figs. S8-S13 and S18, and to define the contribution of pixel (i,j) to tangential vs. radial myosin anisotropy, i.e. $\left[o_{qq}(i,j) - o_{rr}(i,j)\right]m_j(i,j)$. The tangential vs. radial myosin anisotropy in 100×100 μm boxes plotted in Fig. 3H, N and Figs. S12, S13, and S18 is obtained by averaging the contribution of pixels within each box, and normalizing by the average junctional myosin level within the EP (computed for each embryo). As a more complete representation of myosin anisotropy, a myosin anisotropy tensor, whose orientation and magnitude is shown by segments in Figs. S12, S13, and S18, is obtained by averaging and normalizing in the same way the traceless tensor

$$\left(\mathbf{o} - \frac{\mathrm{Tr}\,\mathbf{o}}{2}\mathbf{I}\right)m_j(i,j) \tag{S60}$$

where **I** denotes the identity tensor.

S10. Comparison between the geometry of the margin in model and experiments

We collect here and discuss several elements, appearing at different places in the text and figures, that show the correspondence between the geometry of the embryo margin in model and experiments, and with a boundary of gene expression.

Position of the margin

As noted in the main text and illustrated in Fig. 3M, N and Fig. S13, our cellular-scale analysis of fixed embryos was conducted in embryos that had previously been imaged live for several hours, and show that the centerline of the large-scale, supracellular ring observed at the margin (i.e., the peak of cellular elongation and myosin anisotropy) precisely aligns with the location of the margin determined by our automated fate mapping (from the motion of the tissue). This in turn, as noted in section S7.6, closely coincides with the location of the "embryo contour" that yields the best fit in the model, which is expected since our automated fate mapping is based on the discontinuous deformations at the margin; in the model, these occur along the embryo contour, and the outcome of the model is very sensitive to its position (cf. section S7.9). We also note that the transition between EP and EE, as measured by cell areas in fixed embryos, occurs on the outer edge of the margin (Fig. 3O and Fig. S13), in agreement with the transition between EP and EE in tissue expansion in the model (the dimensionless parameter $r_e \approx 1.14$ in Table S1 places this transition on the outer edge of the margin).

Margin width

The width of the margin, based on the analysis of fixed embryos, shows some variation among embryos, which could reflect inherent variability between embryos, and/or a temporal evolution of the margin width: Movie S8, which shows the dynamics of MyosinII, hints to a gradual narrowing of an initially broad ring. The uniform and constant width that is built into the model is obviously an idealization, since the ring widens posteriorly as it merges into the streak and, possibly, narrows over time. Our best fit for this parameter (standard deviation of the Gaussian profile of 0.12mm, corresponding to a full width at half maximum of 0.28mm) is on the lower end of the experimentally observed widths (Fig. S13), and given that the model is not very sensitive to this parameter (see section S7.9), is fully compatible with experiments.

Correspondence with embryonic territories defined by gene expression

Finally, we note that the location of the embryo margin, as defined by automated fate mapping, closely aligns with the expression boundary of the EP marker Sox3 (Fig. S1K), i.e. the margin, as defined by the motion and mechanical state of the tissue, coincides with the boundary of the EP territory defined by gene expression. Overlaying the deformation map of the tissue onto the pattern of Sox3 expression (Fig. S1L) further demonstrates the association between tissue motion and Sox3 expression, hinting to a connection between fate specification and morphogenesis that remains to be explored.

S11. Alternative models

Here, we contrast our model with alternative hypotheses for the origin of gastrulation movements. Several previous accounts implied that global movements within the epiblast follow passively from the convergent extension of the prospective PS (*1*, *2*). However, they were not backed by an explicit mechanical model. Although a cell-based model was described in (*7*), this

ignored EE tissue altogether, and depended on a confining boundary to shape vortex-like motion within the EP. The models explored in the following show that these proposals, or other conceivable hypotheses, are incompatible with our experimental observations. In particular, models that depend on active force generation in the prospective primitive streak alone, and/or on a confining boundary, fail to account for the precise pattern of motion within the epiblast. We restrict our attention here to models in which motion is driven by active forces within the epiblast. Although gastrulation movements have also been approached as an instance of collective cell migration, such as could be driven by chemotatic cues (*14*), this view is hard to reconcile with the observation that the extracellular matrix underlying the epiblast moves together with the epiblast cells, which implies that the extracellular matrix cannot serve as a substrate for cell migration (*35*).

Although our laser ablation experiments, together with our observations of elongated cells and supracellular actomyosin cables specifically at the embryo margin, confirm that motion in the epiblast is driven by a tensile ring, as suggested by our analysis of tissue flows, we note that the mathematical problem of inferring the pattern of active stresses within the epiblast from its observed motion does not have a unique solution, and one may ask what form other solutions could take.

Our model assumes a uniform tissue viscosity throughout the epiblast, and an even broader set of solutions might be conceived if one allowed for non-uniform tissue mechanical properties. Since motion on either side of the margin is well captured by a passive fluid with uniform viscosity, we restrict our attention here to cases where the viscosity is uniform within the EP and within the EE, but differs between these two territories, e.g. with a more viscous EE acting as a confining boundary for motion within the EP.

In the following, we ignore for simplicity the divergent part of the flow (which is separated from its rotational part in both analysis and model, and makes a limited contribution to the shaping of the embryo), and examine different hypotheses for the origin of its rotational part. To illustrate the outcome of the resulting models, we show in Fig. S20 the patterns of tissue velocity and of the active, passive, and total tissue shear stress computed at a single time point. Since we now allow for non-uniform viscosity, we have departed from the simulation procedure described in section S7.5, and solved the equations of motion using the finite element library FreeFrem++ (*36*). The geometrical parameters of the embryo are taken from the synthetic model, with an epiblast radius corresponding to the intermediate time $t = 4$ h. For simplicity, the approximately circular and centered margin is taken to be exactly so.

Localized vs. distributed active stresses

The key observation that pointed to a tensile margin is the sharp variation in the tissue deformation across the margin, which translates into localized apparent forces along the margin, as inferred from the Laplacian of the velocity field (Fig. 2A). Indeed, tissue on either side of the margin is sheared in opposite directions. Within a fluid-mechanical description, this implies that the lateral margin is subject to passive drag forces from the neighboring tissue on both sides that resist its motion towards the posterior. In our model, these drag forces are balanced by a gradient of active tension *along* the margin. That is, an element of the lateral margin receives a net force towards the posterior because the active tension is higher on its posterior that on its anterior side. Because the length scale of the tension gradient is of the order of the radius r of the EP, our model requires (as noted in section S8.2 and seen in Fig. S20A) that active stresses within the margin exceed the passive stress in the surrounding tissue by a factor of the order of r/w, where

w is the width of the margin - consistent with our observation of higher tissue strains at the margin (Fig. 3A-C). This factor is even larger if we allow for tension in the anterior margin (Fig. S20B), as implied by our laser ablation experiments (Fig. 3A-C).
Any alternative that did not involve localized active stresses in large excess of passive stresses in the surrounding tissue would instead require active stresses in the tissue that surrounds the margin to balance the passive drag forces on the margin. Here, the apparent forces of Fig. 2A would be accounted for by a sharp variation of the active stresses *across* the margin. A trivial solution illustrating this possibility it to set the active stress to the negative of the passive viscous stress at every point, such that the total tissue stress vanishes (Fig. S20C). In other words, each element of the tissue undergoes an autonomous deformation driven by active stresses within that element, with no force transmission across the tissue. Although mathematically conceivable, such a model is hardly plausible, as it would require a tight coordination across the epiblast to produce an apparently passive velocity field outside the margin (with a Laplacian that is close to zero, cf. Fig. 2A). But most importantly, any such solution, depending on distributed rather than localized active stresses, would be inconsistent with the localized tissue strains observed in our laser ablation experiments, and with our observations of elongated cells and actomyosin cables specifically at the margin.
Different solutions could be conceived if one allowed for a non-uniform viscosity. In particular, discontinuous strain rates across the margin could result from a step in viscosity, with no need for localized forces. However, this would not explain that the tissue is sheared in opposite directions on either side of the margin. To turn the argument around, even with different viscosities, the tissue on both sides of the lateral margin would still exert a passive drag force that resists its posterior-ward motion, requiring active forces to satisfy force balance.

Sustained tension at the margin vs. localized convergent extension
Coming from a different angle, the need for sustained tensions along the margin is obvious when one compares tissues flows in our model with a model that would rely solely on convergent extension of the prospective PS. At early times, the two models would not much differ, since the site of active stresses in our model largely overlaps with the initial location of the prospective PS (a crescent-shape domain along the posterior margin, cf. Fig. 2H). Over time, however, the primitive streak becomes more compact, before extending along the A-P axis. In our model, the spatial distribution of active stresses is essential to drive motion in two counter-rotating vertices. This pattern of motion would be lost as the prospective PS changes shape, as illustrated by Fig. S20D, which shows the motion driven by radially symmetric pattern of active stress (corresponding to an intermediate stage in convergent extension of the prospective PS). Here, tissue converges toward the A-P axis and diverges along it, forming four vortices because motion is confined by the epiblast border (similar to a flow structure that was proposed previously to describe gastrulation movements (*38*)). Although the vortices are stronger in the anterior than in the posterior, which is closer to the epiblast border, this still markedly differs from motion in the epiblast at that stage. In addition to being inconsistent with the qualitative structure of motion in the epiblast, such a model would also not explain the sustained apparent forces at the margin (Fig. 2A), and anisotropic strains revealed by laser ablations (especially in the anterior margin; Fig. 3A-C).

Localized convergent extension and non-uniform viscosity

Following the suggestion that gastrulation movements are shaped by a confining boundary (*7*), the same active stress distribution could give rise to only two vortices if EE tissue has a higher viscosity, as shown in Fig. S20E. Here, the variation of viscosity across the margin is described by the same function and parameter values that are used in the synthetic model to define a smooth transition between EP and EE and describe differential expansion of the epiblast (Eq. S40 and Table S1). The resulting pattern of motion exhibits only two vortices, but is inconsistent with our observation that tissue velocity is greatest near the margin and gradually decays away from it. Here, instead, the velocity quickly drops near the margin and in the EE tissue, consistent with EE tissue acting as a boundary.

One might consider an alternative hypothesis where the viscosity is instead higher *inside* the EP, such that forces generated by the contracting PS are preferentially transmitted within the EP to drive its motion, with a limited resistance from the EE. But this exacerbates vortex-like motion posterior to the embryo, resulting in a pattern of motion that even further departs from that observed in the epiblast (Fig. S20F).

Taken together, this shows that previous accounts of gastrulation movements fail to account for the precise pattern of motion within the epiblast, which must arise from a tensile ring - as directly observed in our experiments.

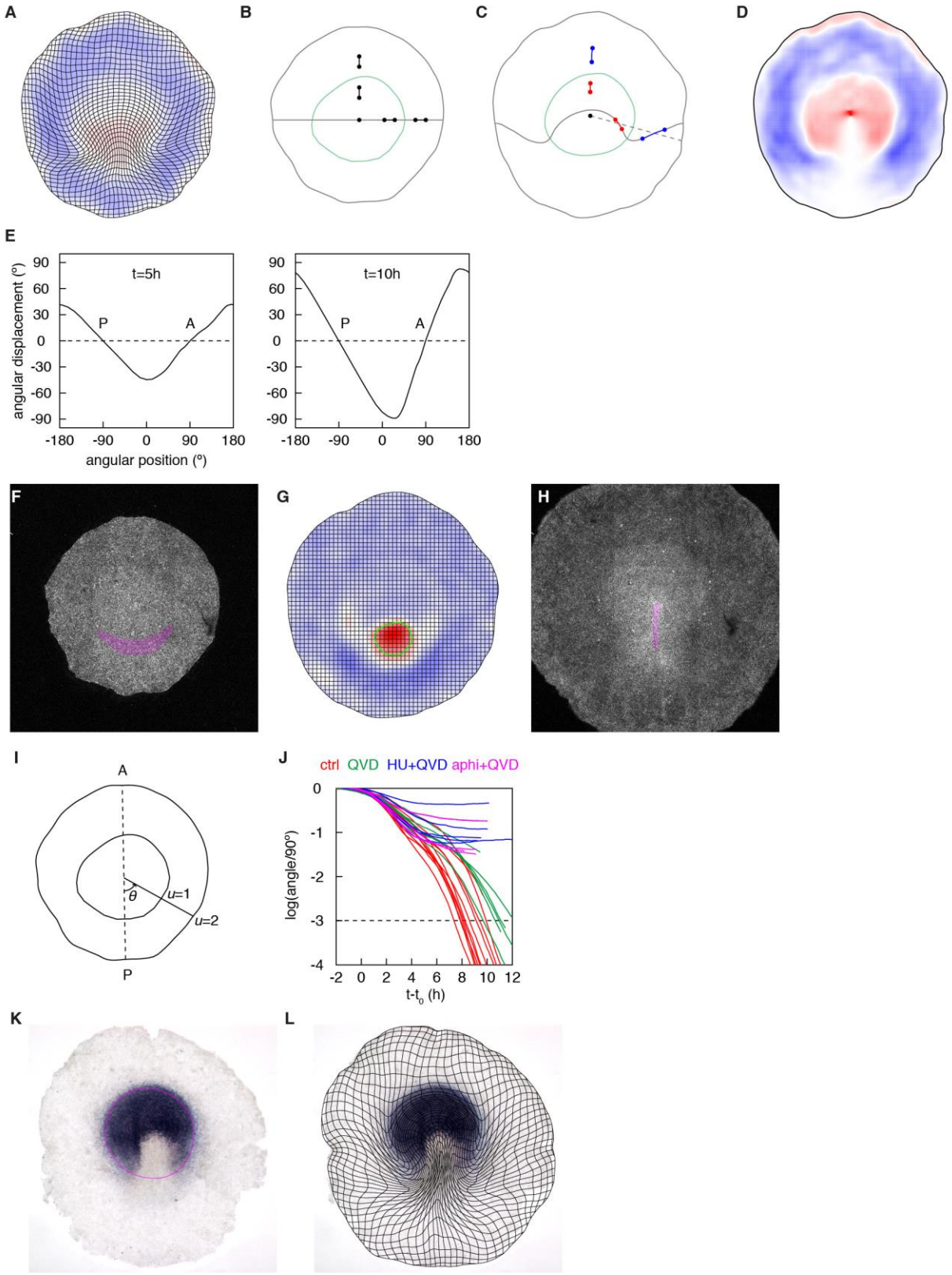

Figure S1. Automated fate mapping and spatiotemporal registration. (**A**-**D**) Embryo proper. **A**, Deformation of the tissue over a 4 h interval. **B**, **C**, An initially straight line, and segments on

either side of the margin (green) are tracked over the same time interval, showing: on the right-hand side, differential rotation relative to a radial line (dotted line in **C**); in the anterior, differential length changes (red and blue denote interior and exterior as in **D**). **D**, Plot of the criterion function used to identify the embryo margin (red, interior; blue, exterior). (**E**) Anterior-posterior axis. Plots of the angular displacement of points along the embryo margin, as a function of initial angular position (relative to the horizontal image axis), over intervals of 5 and 10 h. The anterior (A) and posterior (P) are identified as zero crossings of the angular displacement. (**F**-**H**) Prospective primitive streak. **F**, **H** are two images of an embryo at the onset of motion and at the "streak stage", respectively, while **G** shows the area changes between an intermediate stage and **H**, similar to Fig. 1C. The boundary of the prospective primitive streak is identified by thresholding the area changes (green line in **G**). The corresponding regions are highlighted in **F**, **H** (magenta). (**I**) Coordinate system for spatial registration. (**J**) Contraction of a 90º posterior sector vs. time, used for temporal registration, in control and treated embryos (the dashed line defines the "streak stage"). (**K**, **L**) Comparison with expression of the ectodermal/EP marker Sox3. The embryo margin determined by automated fate mapping (magenta line in **K**) aligns with the boundary of the Sox3 expression domain in an embryo that was fixed after live imaging. The tissue deformation map overlaid with the same image in **L** further demonstrates the association between tissue motion and Sox3 expression; the emergent PS, from which Sox3 is excluded (*37*), is visible here as the region undergoing convergent extension.

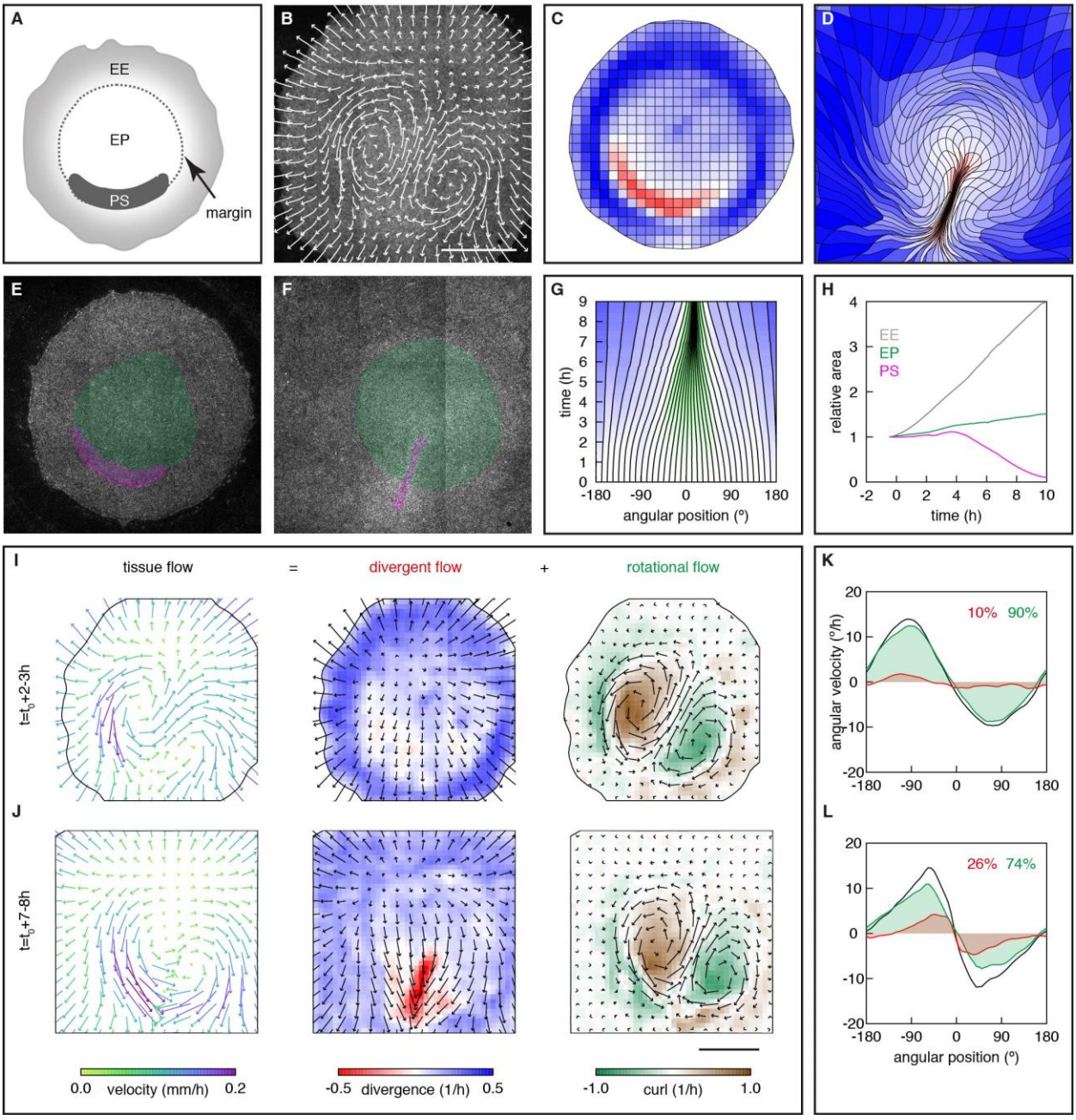

Figure S2. Quantitative description of gastrulation movements of an embryo imaged directly in the egg, without *ex vivo* culture. (Similar analysis as in Fig. 1). (**A**) Anatomical description of the early epiblast (EE, extra-embryonic territory; PS, prospective primitive streak; EP, embryo proper). (**B**-**D**) Trajectories (**B**, *t* = 3.5-5.5 h) and deformation of an initially square grid (**C**, **D**), from the PIV analysis of a memGFP embryo movie (colors in **C**, **D** show area changes between the initial (**C**, *t* = 0**)** and final (**D**, *t* = 9 h**)** configurations). (**E**-**H**), Automated fate mapping (green, EP; magenta, PS; **E**, *t* = 0 h; **F**, *t* = 9 h); **G,** time evolution of angular positions; **H**, area of tissue regions vs. normalized time. (**I**-**L**) Decomposition of the tissue velocity field into divergent and rotational components (**I**, **J**), and contributions to motion along the margin (**K**, **L**) (averages over the indicated time intervals). Scale bars, 1 mm.

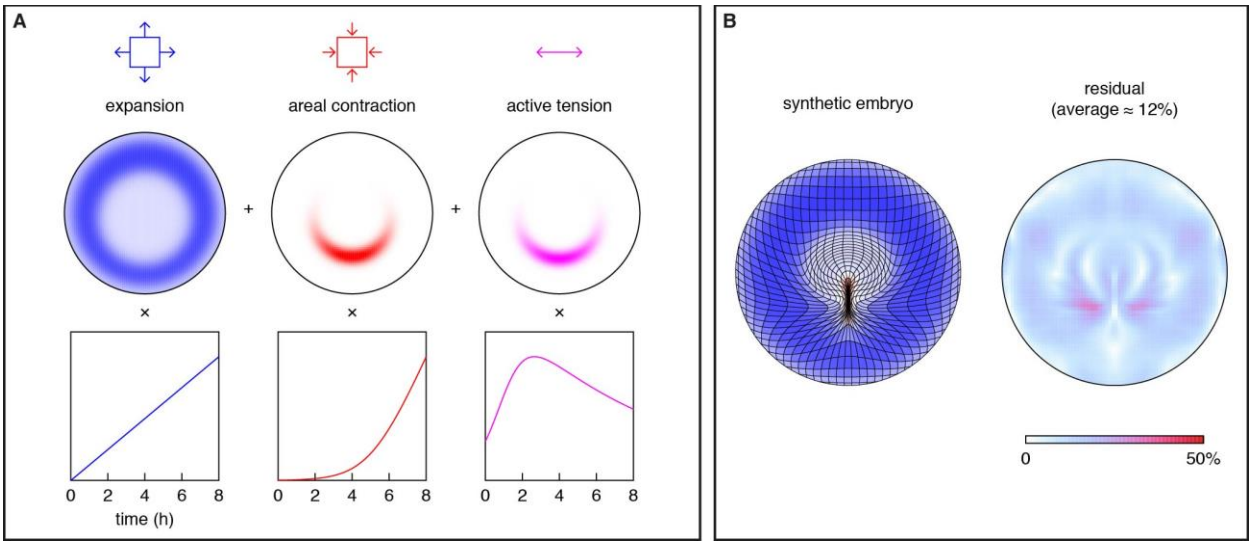

Figure S3. A synthetic model. (**A**), EE expansion, areal contraction of the prospective primitive streak, and tension along the margin as a function of space and time used to build a synthetic model of gastrulation. (**B**) Deformation map for the synthetic model and deviation from average embryo. Scale bars, 1 mm.

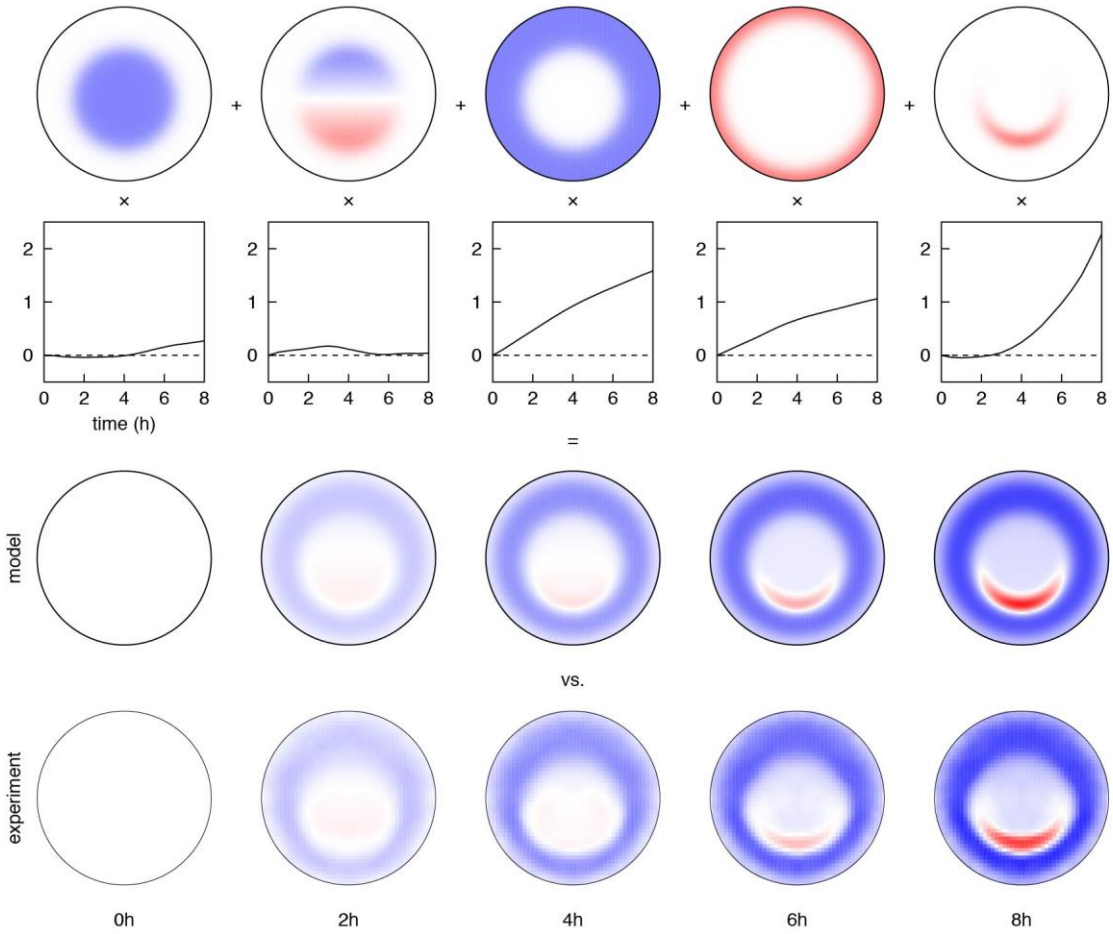

Figure S4. Detailed model for area changes. The log of area changes in the tissue is modeled as a linear combination of five modes, from left to right: uniform and graded expansion within the EP, EE expansion, reduced expansion near the tissue border, and areal contraction of the prospective primitive streak. Amplitudes vs. time are plotted below each mode, and the resulting area changes are compared to experimental area changes (from a symmetrized, average embryo) at successive times (colors as in Fig. 1C).

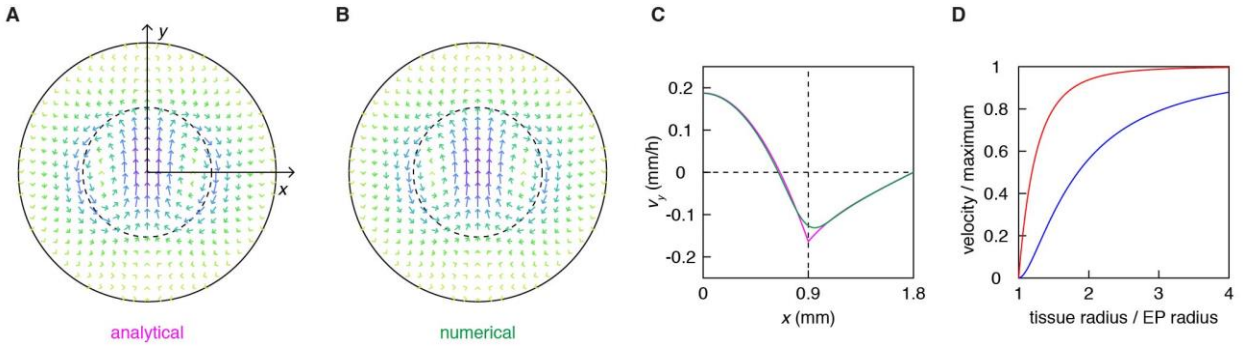

Figure S5. Analytical model (**A**) Velocity field computed analytically in the limit of a vanishing margin width, with a sinusoidal tension profile, $T / m = \cos q$, cf. equation (S47) (dashed line, margin; solid line; tissue border). (**B**) Velocity field computed numerically with the same tension profile but a finite margin width, w = 0.1 mm, cf. equation (S34). (**C**) Comparison between the analytical and numerical velocity profiles as a function of distance to the center, showing that the two profiles differ appreciably only near the margin (dashed line); the slope becomes discontinuous in the limit of a vanishing margin width. (**D**) Analytical curves showing how the global ("swimming") velocity of the embryo (blue) and relative movement within the embryo (red) depend on the total size of the tissue relative to the EP. Motion within the embryo, thus the progress of gastrulation, is predicted to be much less sensitive to the presence of the tissue border, tending more rapidly to its maximum value.

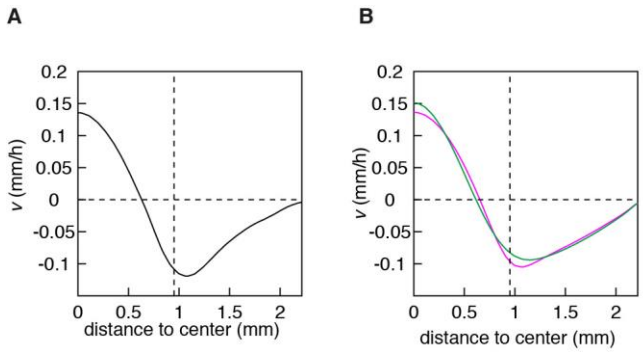

Figure S6. Velocity profiles in experiments and model. (**A**) Experimental profile of orthoradial velocity along a line perpendicular to the axis of the average embryo, at the intermediate time t = 4 h (cf. Fig. 2F), showing a sharp change in slope at the margin (dotted line). (**B**) The same profile in our main model (magenta; cf. Fig. 2E), and from a fit of the model with the margin width fixed to a larger value (w = 0.3 mm instead of 0.12 mm; green), showing a much smoother transition with a wider margin; although global motion in the model is not very sensitive to the width of the margin (cf. section S7.9), values much larger than that inferred from the fit are inconsistent with this local feature of tissue motion.

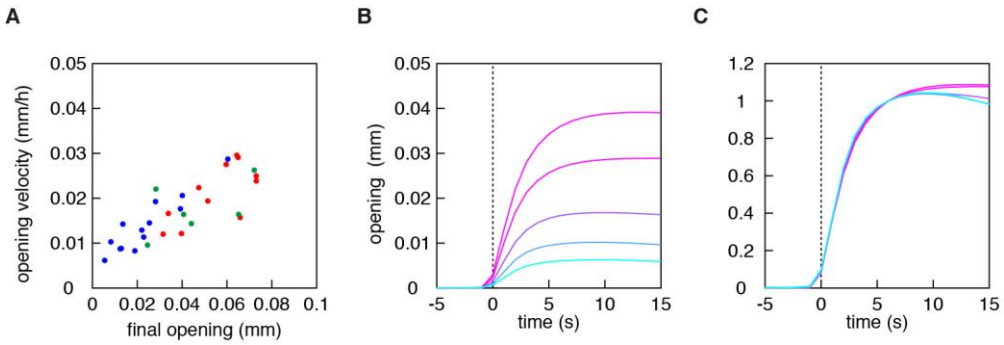

Figure S7. Time-resolved response to linear laser cuts. (**A**) PIV tracking of tissue motion following 250 µm radial cuts performed at different locations in the epiblast (colored coded as in Fig. 3B, C; red, posterior margin; green, anterior margin; blue, EP) shows a strong correlation between initial opening velocity and final opening (Pearson correlation coefficient $r = 0.78$). (**B-C**) The opening at increasing distances from the cut (from top to bottom in **B**: 25 µm as in A, 100, 200, 300, and 400 µm; rescaled to opening at 6 s in **C**) shows simultaneous motion at different distances, arguing against a role for friction.

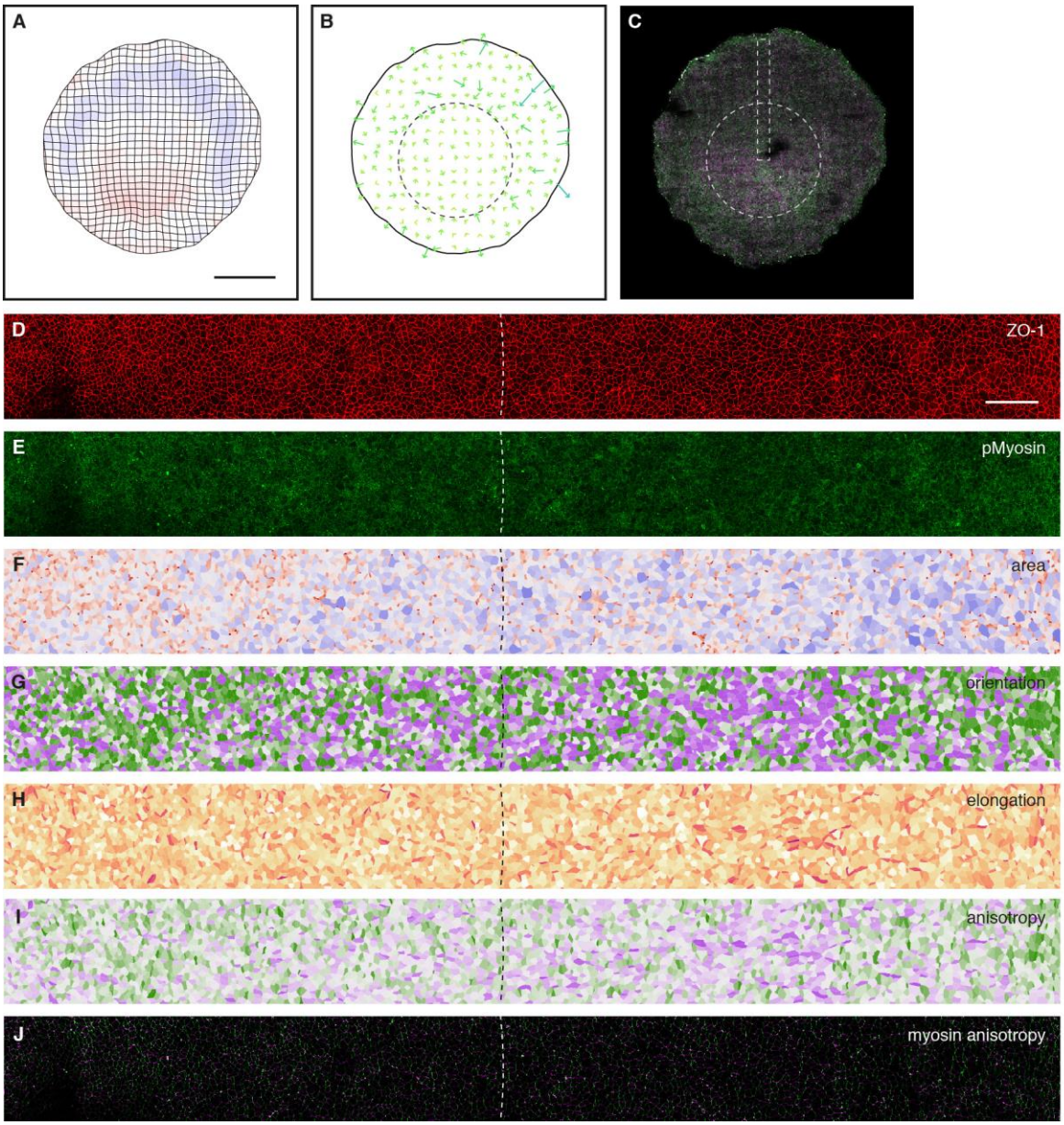

Figure S8. Quantification of cell shape and phosphorylated Myosin anisotropy in an anterior portion of an early embryo. (**A**-**C**) Deformation map (**A**) and apparent forces (**B**; dotted line, margin) from live imaging of an early embryo ($t \gg t_0$), and junctional myosin in the same embryo after fixation (**C**; colors denote orientation; magenta, radial; green, orthoradial). (**D**-**J**) ZO-1 (**D**) and phospho-Myosin (**E**) immunofluorescence used to segment and quantify cell areas (**F**), cell orientation (**G**), cell elongation (**H**), cell shape anisotropy (**I**) and junctional phosphoMyosin anisotropy (**J**; colors as in **C**) of the region boxed in **C** (see Supplementary Text). Scale bars, **A**, 1 mm, **D**, 100 µm.

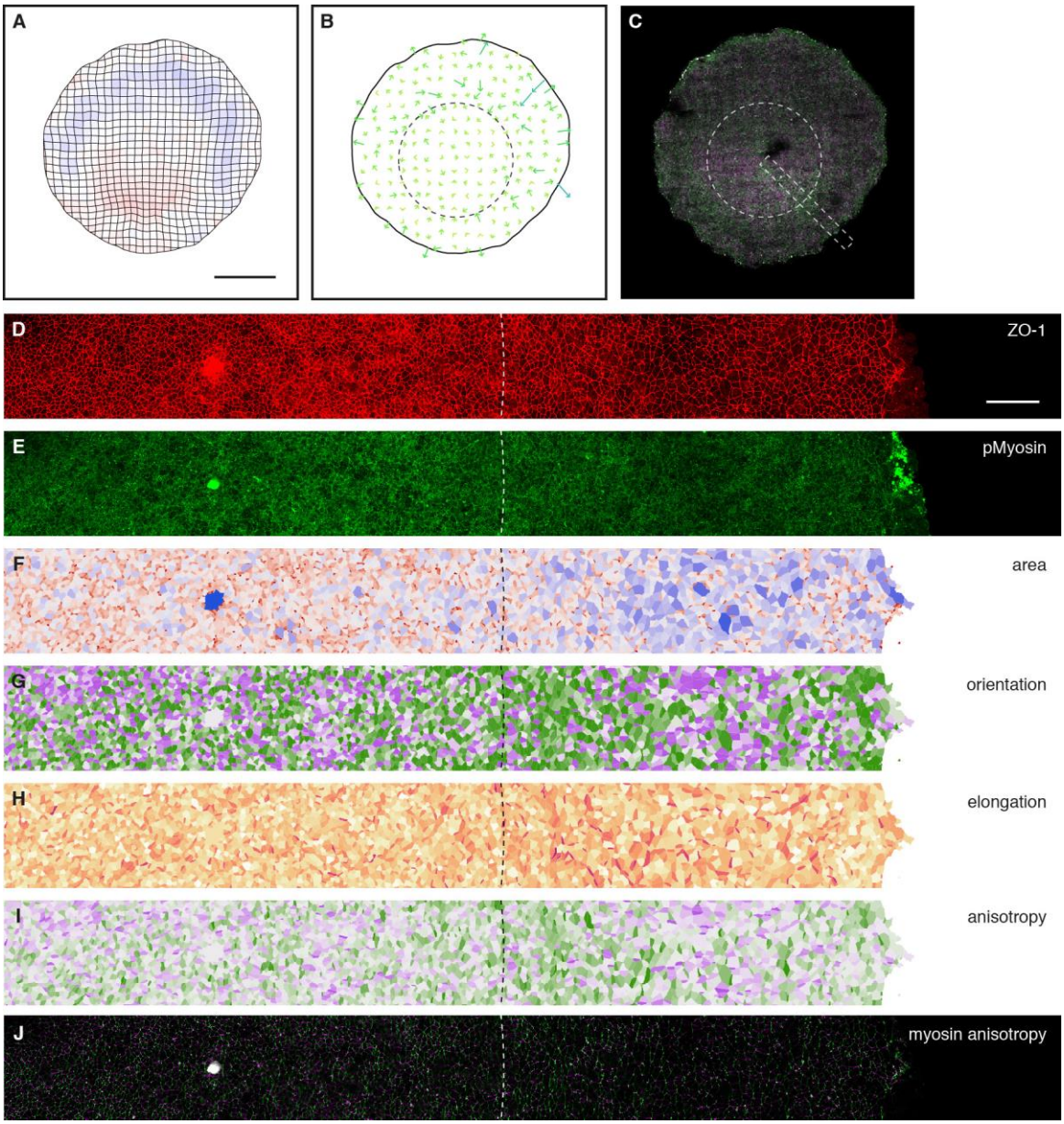

Figure S9. Quantification of cell shape and phosphorylated Myosin anisotropy in a posterior portion of an early embryo. (A-C) Deformation map (**A**) and apparent forces (**B**; dotted line, margin) from live imaging of an early embryo ($t \gg t_0$), and junctional myosin in the same embryo after fixation (**C**; colors denote orientation; magenta, radial; green, orthoradial). (**D-J**) ZO-1 (**D**) and phospho-Myosin (**E**) immunofluorescence used to segment and quantify cell areas (**F**), cell orientation (**G**), cell elongation (**H**), cell shape anisotropy (**I**) and junctional phosphoMyosin anisotropy (**J**; colors as in **C**) of the region boxed in **C** (see Supplementary Text).

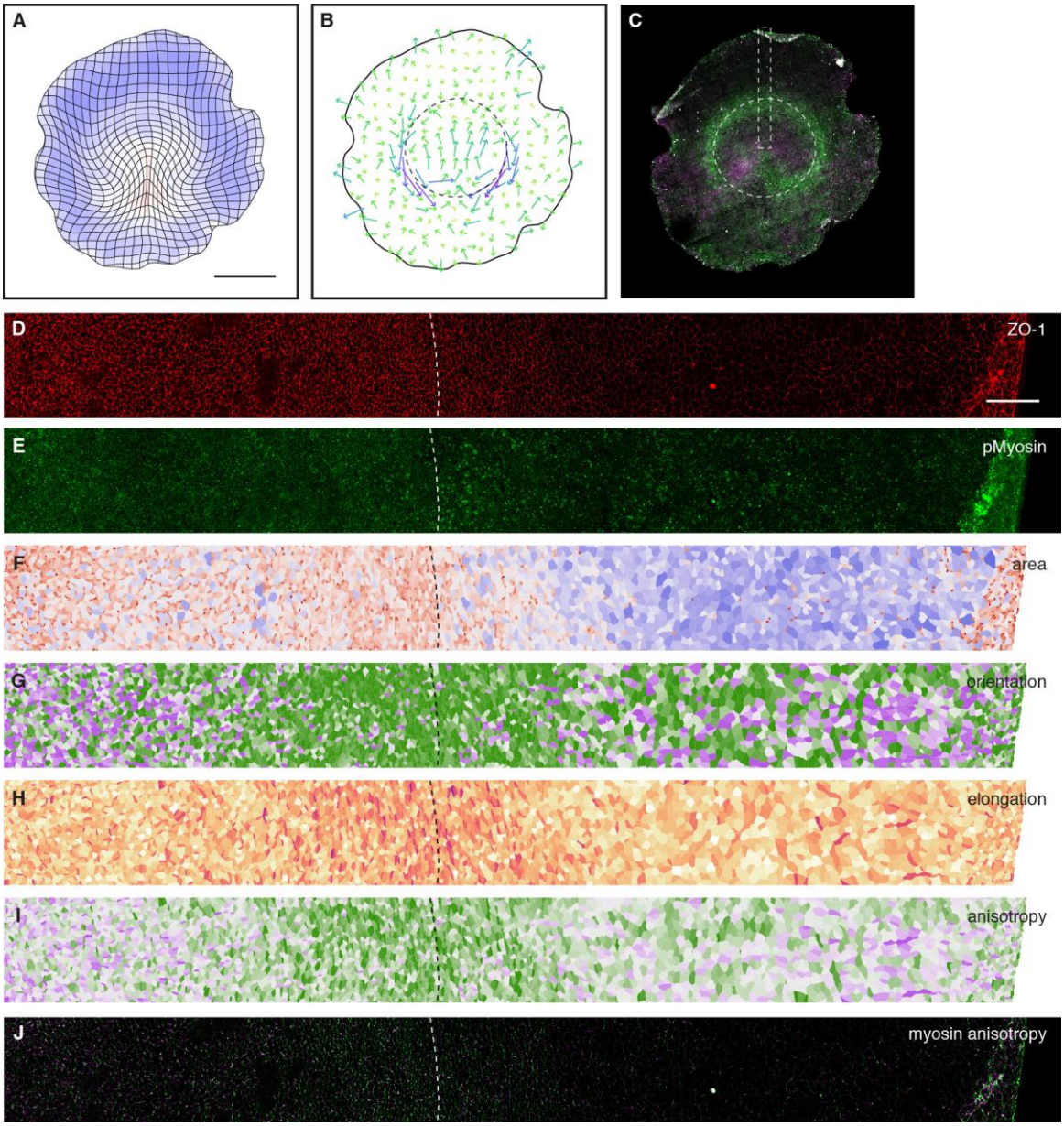

Figure S10. Quantification of cell shape and phosphorylated Myosin anisotropy in an anterior portion of an intermediate-stage embryo. (A-C) Deformation map (**A**) and apparent forces (**B**; dotted line, margin) from live imaging of an intermediate-stage embryo ($t \approx t_0 + 4$ h), and junctional myosin in the same embryo after fixation (**C**; colors denote orientation; magenta, radial; green, orthoradial). **(D-J)** ZO-1 (**D**) and phospho-Myosin (**E**) immunofluorescence used to segment and quantify cell areas (**F**), cell orientation (**G**), cell elongation (**H**), cell shape anisotropy (**I**) and junctional phosphoMyosin anisotropy (**J**; colors as in **C**) of the region boxed in **C** (see Supplementary Text).

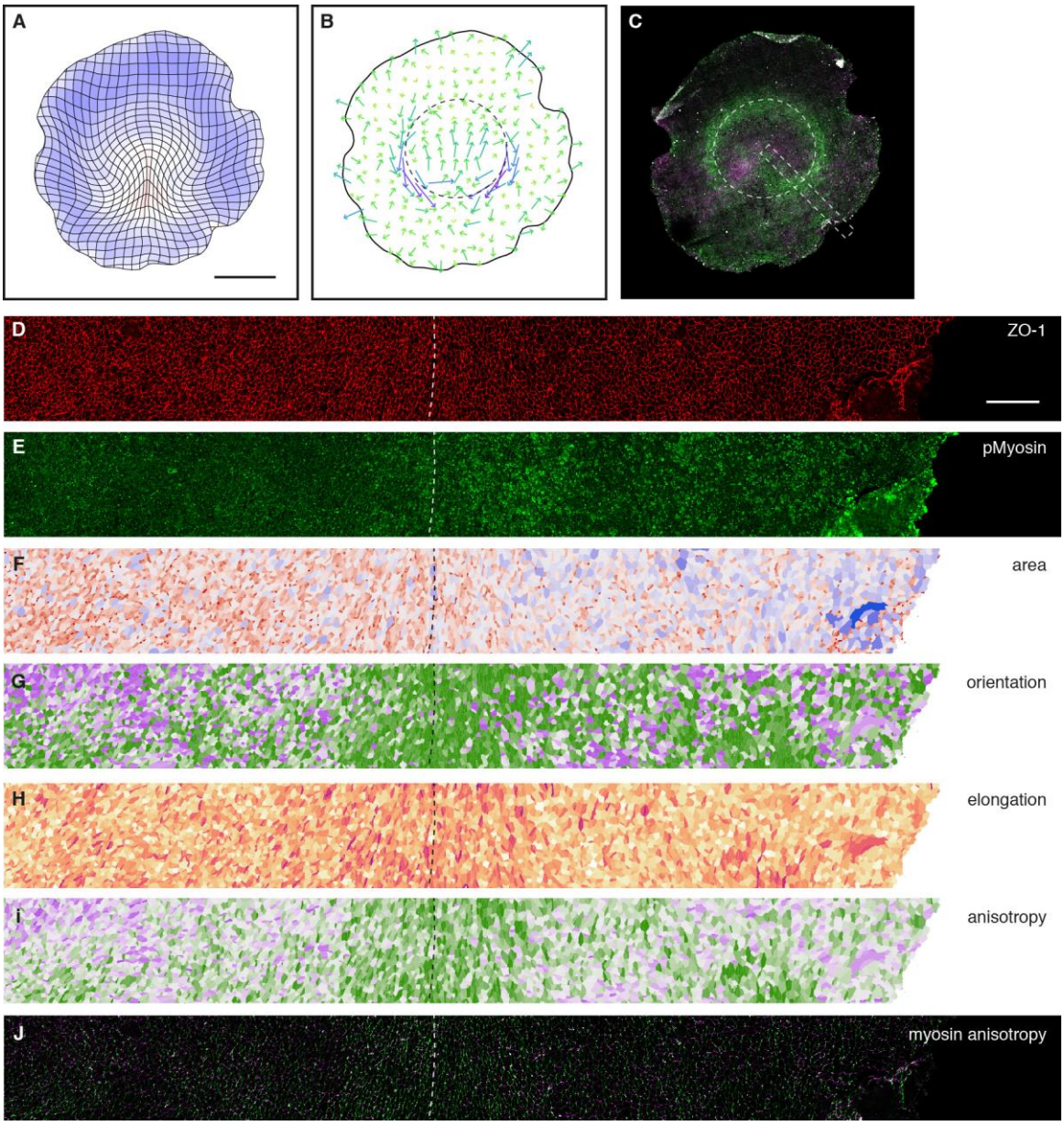

Figure S11. Quantification of cell shape and phosphorylated Myosin anisotropy in a posterior portion of an intermediate-stage embryo. (A-C) Deformation map (**A**) and apparent forces (**B**; dotted line, margin) from live imaging of an intermediate-stage embryo ($t \approx t_0 + 4$ h), and junctional myosin in the same embryo after fixation (**C**; colors denote orientation; magenta, radial; green, orthoradial). (**D-J**) ZO-1 (**D**) and phospho-Myosin (**E**) immunofluorescence used to segment and quantify cell areas (**F**), cell orientation (**G**), cell elongation (**H**), cell shape anisotropy (**I**) and junctional phosphoMyosin anisotropy (**J**; colors as in **C**) of the region boxed in **C** (see Supplementary Text).

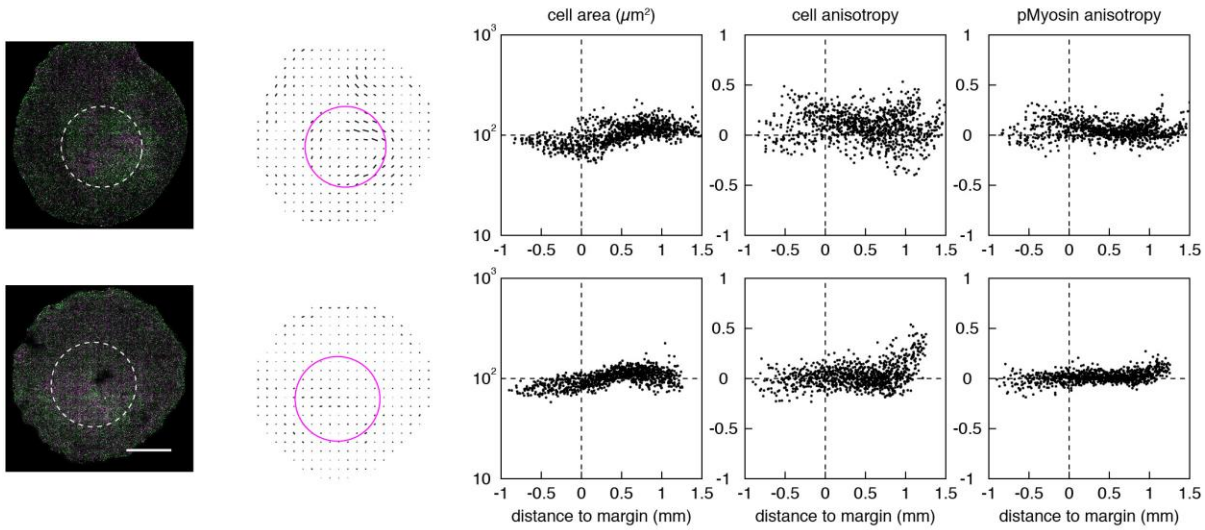

Figure S12. Cellular-scale analysis of early embryos. Analysis of control embryos that were lived imaged and fixed shortly after movement initiation, showing the distribution of junctional phosphorylated Myosin (colored by orientation; magenta, radial; green, tangential) and its anisotropy (segments show the orientation and magnitude of Myosin anisotropy in 200×200 μm boxes), and scatter plots of cell area, tangential vs. radial cell shape anisotropy, and tangential vs. radial Myosin anisotropy averaged in 100×100 μm boxes (excluding a 90º posterior sector as in Fig. S13). The approximate location of the embryo margin (dashed circles in the images) was determined based on the pattern of areal expansion/contraction (cf. Fig S7A; our automated fate mapping cannot be applied at this early stage). Displayed quantities are defined in Supplementary Text. Scale bar, 1 mm.

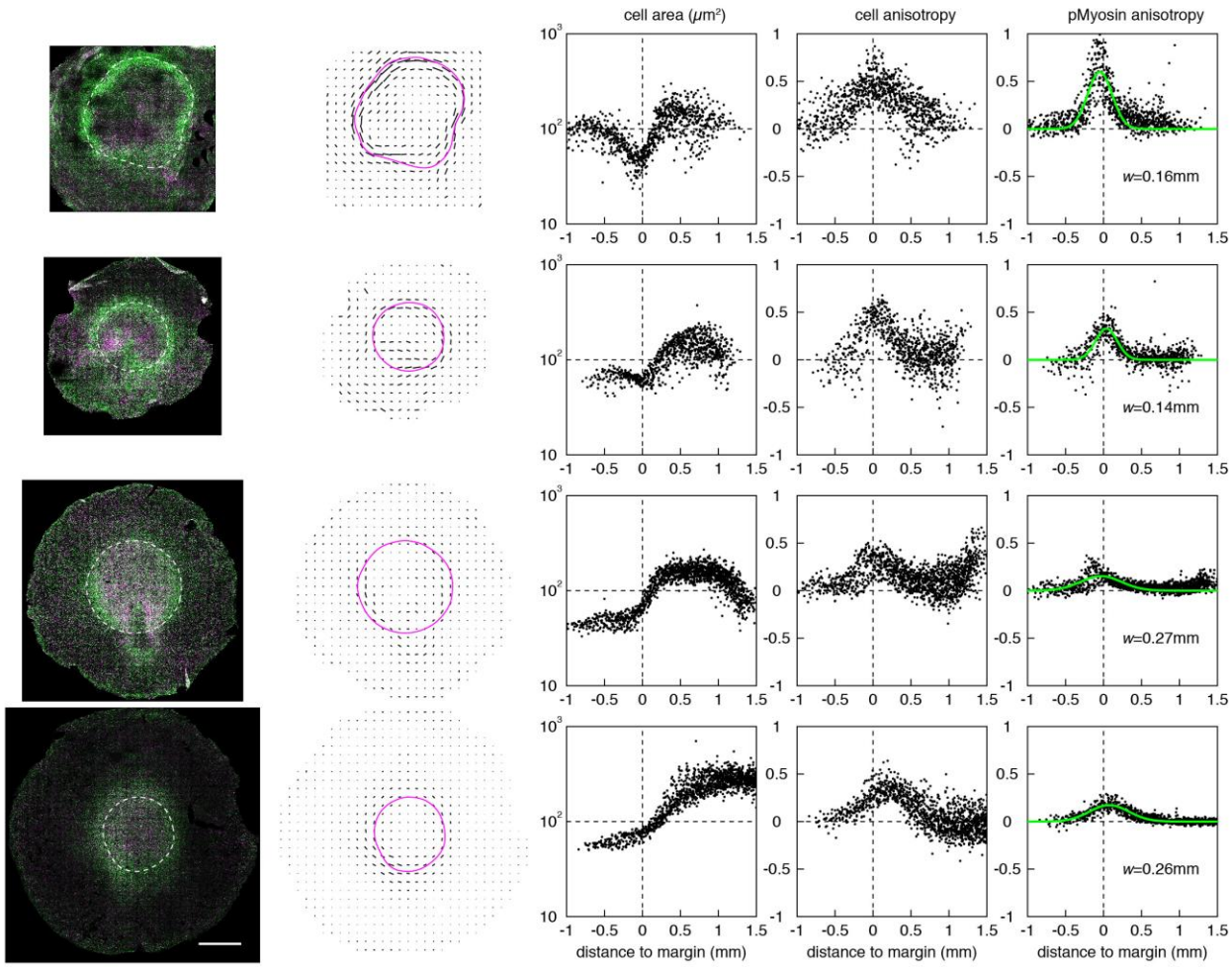

Figure S13. Cellular-scale analysis of intermediate-stage embryos. Analysis of control embryos that were live imaged then fixed at an intermediate stage (~ 4 h after movement initiation), showing the distribution of junctional phosphorylated Myosin (colored by orientation; magenta, radial; green, tangential) and its anisotropy (segments show the orientation and magnitude of Myosin anisotropy in 200×200 μm boxes), and scatter plots of cell area, tangential vs. radial cell shape anisotropy, and tangential vs. radial Myosin anisotropy averaged in 100×100 μm boxes (excluding a 90º posterior sector that contains the prospective primitive streak). Dashed lines in the images show the location of the embryo margin from automated fate mapping (based on motion before fixation; as an exception, live and fixed images of the embryo in the first row, possibly distorted upon fixation, did not align well and the location of the margin was determined from the fixed image; this embryo was excluded from the average of Fig. 3O). Green curves show Gaussian fits with standard deviation *w* as indicated. Displayed quantities are defined in Supplementary Text. Scale bar, 1 mm.

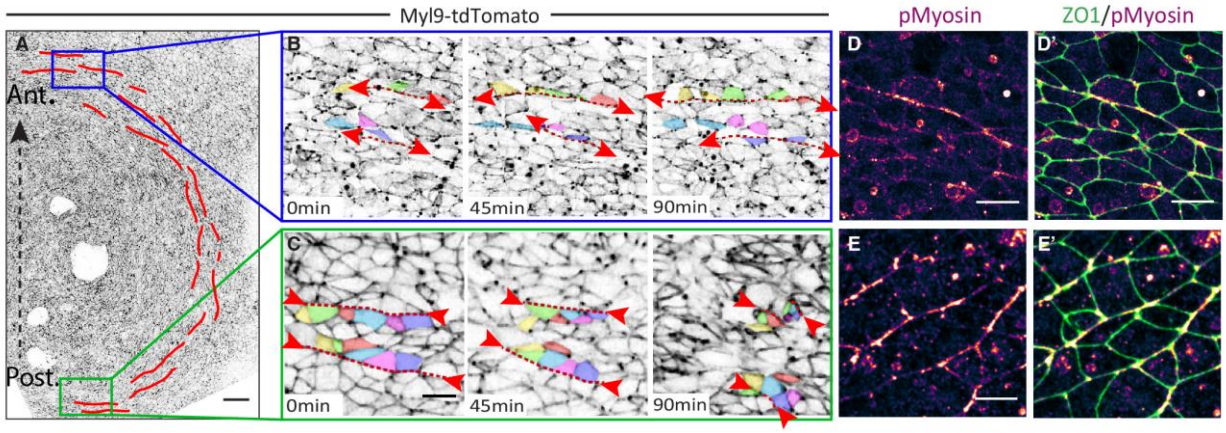

Figure S14. Supracellular cables at the embryo margin. (**A**-**C**) Time series from Movies S8 and S9 showing supracellular actomyosin cables (red) at the margin in a Myl9-tdTomato transgenic embryo and concomitant cell behavior (tracked colored cells) at the anterior (**B**) and posterior (**C**) margin. Actomyosin cables extend anteriorly and contract posteriorly (arrowheads). (**D, E**) Antibody staining for phosphorylated Myosin and ZO-1 in the anterior (**D**, **D'**) and posterior (**E**, **E'**) margin revealing orthoradial supracellular cables. Scale bars, **B**, **C**, 20 µm; **D, E**, 10 µm.

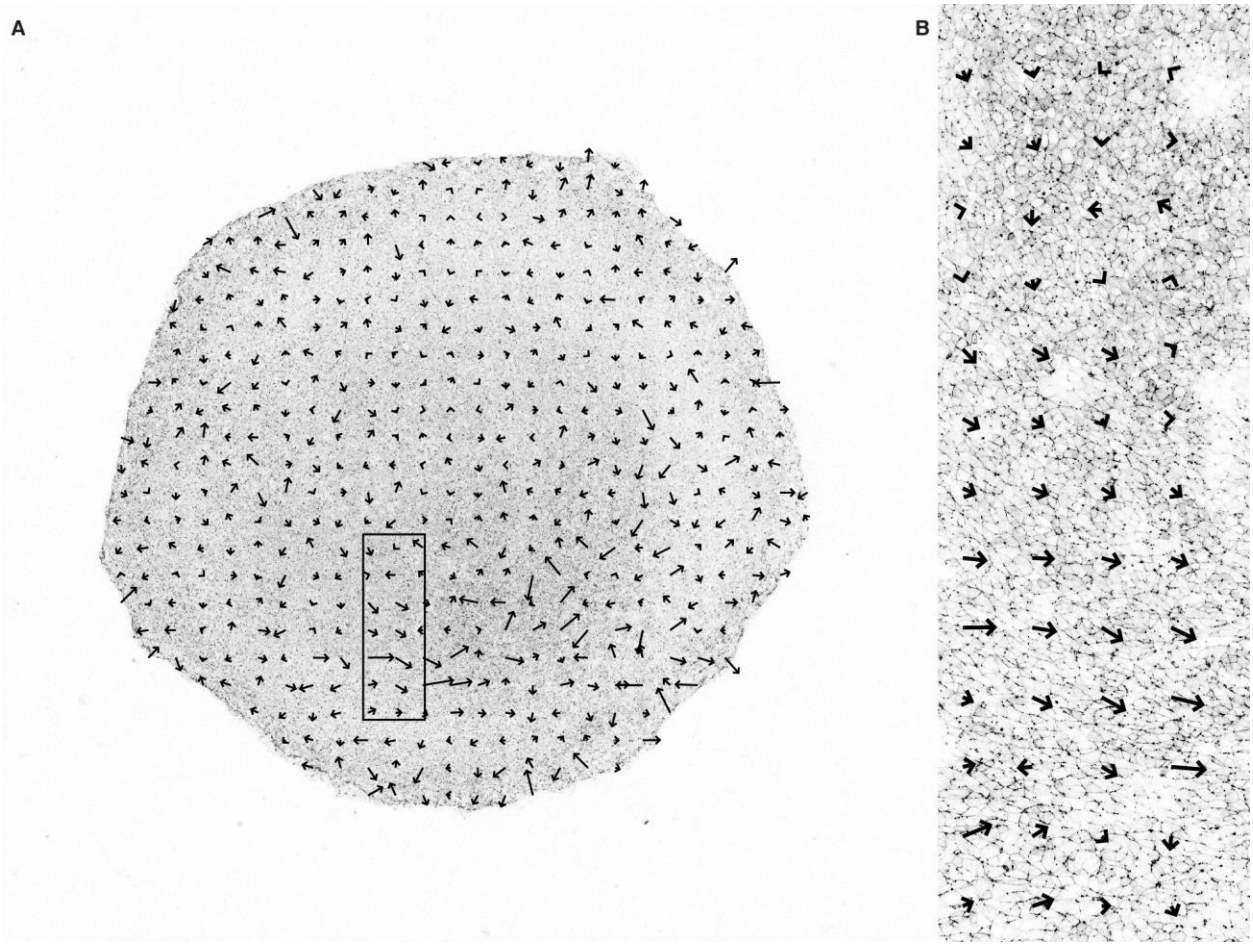

Figure S15. Correlation between supracellular cables and apparent forces inferred from tissue motion. (**A**) Apparent forces inferred from tissue motion, from a movie of a tdtomato-Myl9 embryo imaged at low resolution (using a 10x objective) in its entirety. (**B**) The same apparent forces, overlaid onto a high-resolution snapshot (using a 40x objective) of the boxed region in **A** (0.35×1.06 mm) show the overlap between the location of apparent forces and a region with elongated cells and alignment of junctions into supracellular cables.

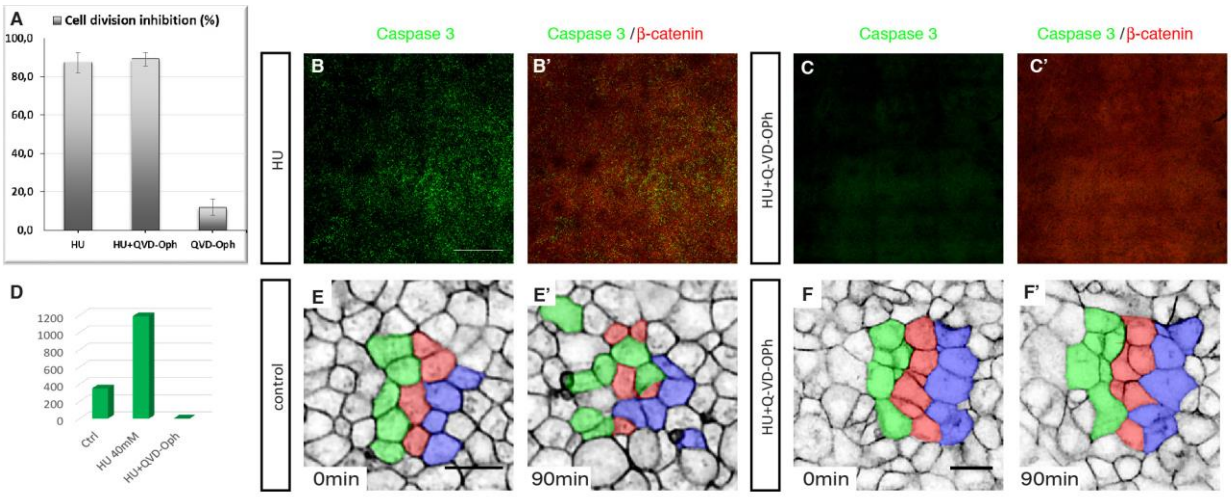

Figure S16. Cellular-scale effect of cell division and apoptosis inhibition. (**A**) Percentage of cell division inhibition in drug treated embryos. (**B-D**) Embryos treated with HU (**B**, **B**') or with HU+Q-VD-OPh (**C**, **C**'), stained for caspase 3 (green), which labels apoptotic cells, and counterstained with beta-catenin (red). The number of caspase 3 positive cells for each condition is quantified in **D**. (**E**, **F**) Effect of cell division on cell rearrangements revealed by cell dispersion in control (**E**, **E'**) and treated (**F**, **F'**) embryos. Scale bars, **B**, 500 µm; **E**, **F**, 20 µm.

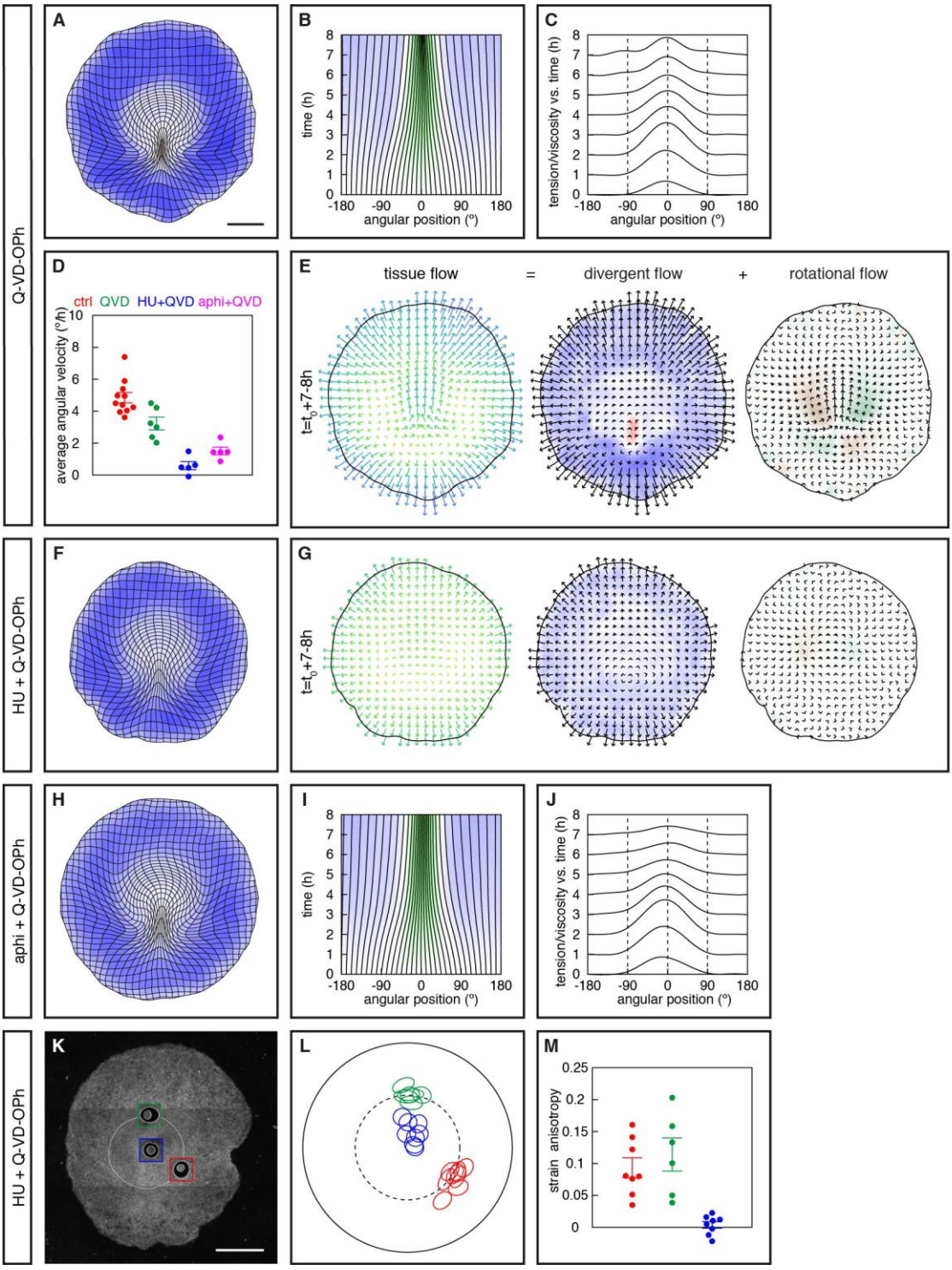

Figure S17. Tissue-scale effect of cell division and apoptosis inhibition. (**A**-**J**) Effect of Q-VD-OPh alone, HU+Q-VD-OPh, and aphidicolin+Q-VD-OPh on gastrulation movements. **A**, **F**, **H**, Deformation maps (average embryos; n = 5 embryos each). **B**, **I,** Time evolution of angular positions (average embryos; cf. Fig. 4B). **C**, **J**, Tension/viscosity profiles from model fit to average embryos (cf. Fig. 4C). **D**, Average angular velocity along the margin at $t = t_0 + 6.5$-7.5 h. **E**, **G**, Decomposition of the tissue velocity field into divergent and rotational components

(averages over embryos). (**K**-**M**) 250 μm circular laser cuts in a single memGFP embryo (**K**) and representation of all laser cut experiments (**L**) for which the response was quantified (**M**; bars, mean ± SE) (red, posterior margin; green, anterior margin; blue, EP). Scale bars, 1 mm.

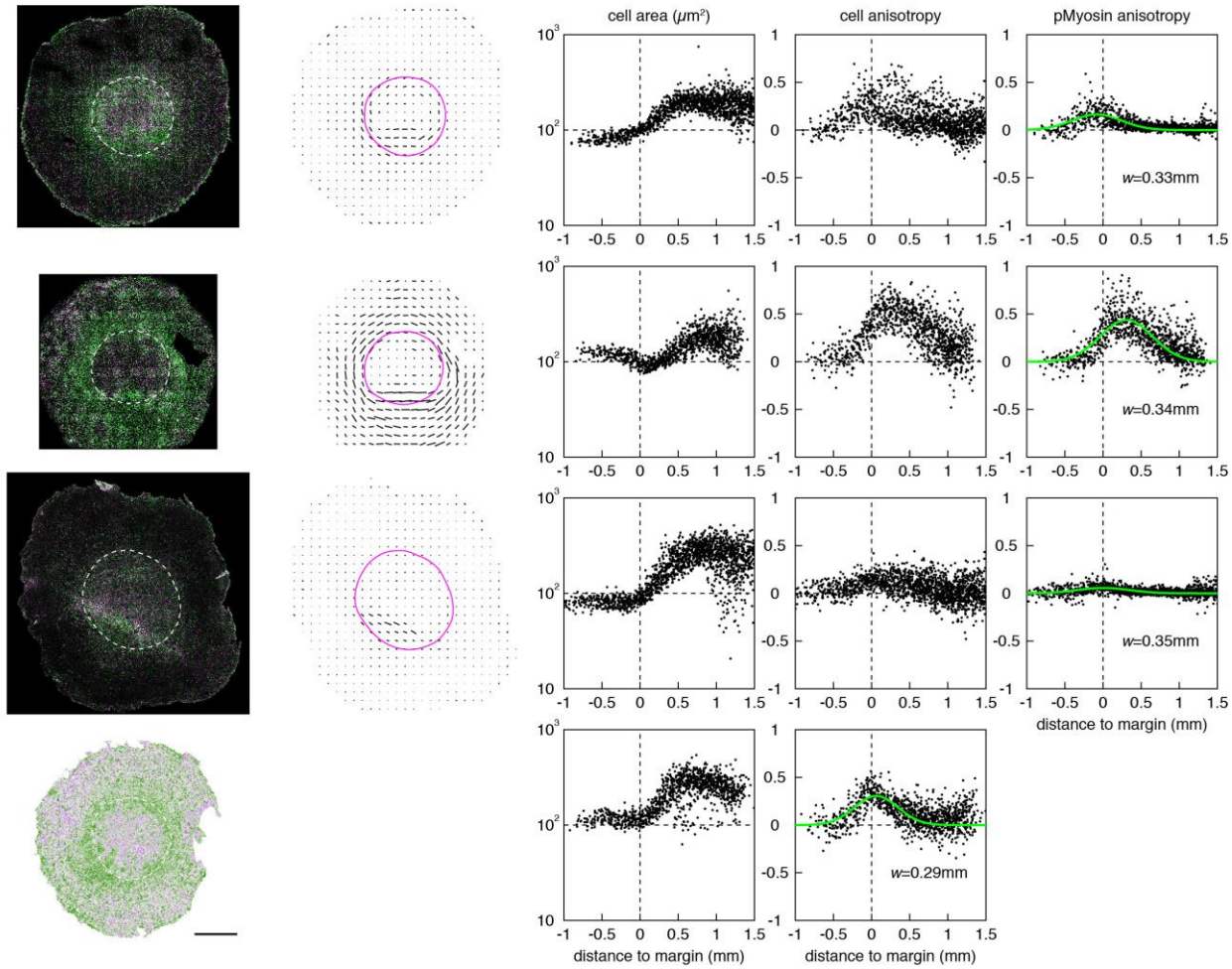

Figure S18. Cellular-scale analysis of HU+QVD-O-Ph-treated embryos. Analysis of HU+QDV-O-Ph treated embryos that were live imaged then fixed, showing the distribution of junctional phosphorylated Myosin (colored by orientation; magenta, radial; green, tangential) and its anisotropy (segments show the orientation and magnitude of Myosin anisotropy in 200×200 μm boxes), and scatter plots of cell area, tangential vs. radial cell shape anisotropy, and tangential vs. radial Myosin anisotropy averaged in 100×100 μm boxes (excluding a 90º posterior sector as in Fig. S13). Dashed lines in the images show the location of the embryo margin from automated fate mapping (based on motion before fixation). Green curves show Gaussian fits with standard deviation *w* as indicated. As an exception, the embryo in the last row was not stained for phosphorylated Myosin and the left-hand panel shows instead tangential vs. radial cell shape anisotropy as in Fig. 3L. Displayed quantities are defined in Supplementary Text. Scale bar, 1 mm.

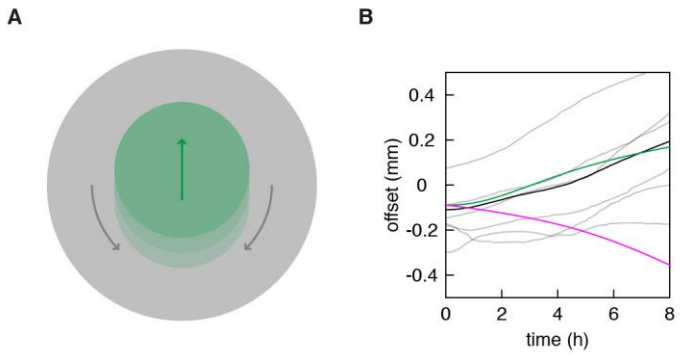

Figure S19. The embryo as a swimmer. (**A**) Sketch of swimming motion (green arrow) induced as the EP (green) draws EE tissue (gray) posteriorly (gray arrows). (**B**) Anterior movement of embryos relative to tissue border (gray, n = 6 embryos; black, average embryo; green, synthetic embryo; magenta, synthetic embryo without active tensions). In the absence of active tensions, the initially off-centered embryo is predicted to drift posteriorly, i.e. the embryo swims against a current associated with tissue expansion.

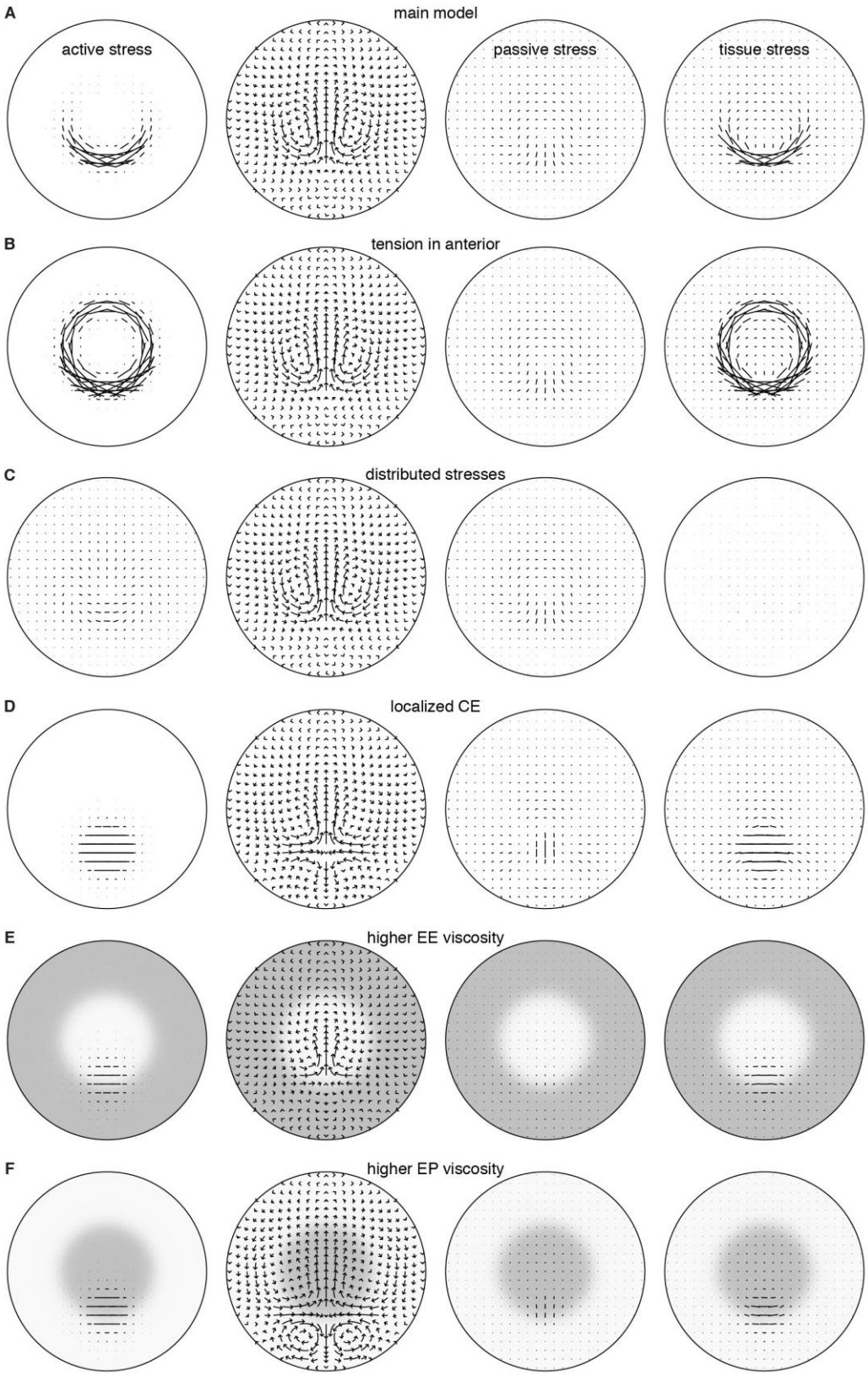

Figure S20. Alternative models for gastrulation movements. Different hypotheses for the origin of tissue motion in the epiblast are illustrated by the pattern of active shear stress driving

motion, and the resultant tissue velocity field and patterns of passive and tissue (active plus passive) shear stress (segments show the orientation and magnitude of shear stress). For simplicity, area changes are not considered, i.e. the velocity fields are divergence-free. The viscosity of the tissue is uniform in **A-D** and non-uniform in **E**, **F**. (**A**) A simplified version of our synthetic model with a circular, centered margin. (**B**) Same as **A** with a uniform tension added along the margin, such that the tension in the anterior is a third of the tension in the posterior. This leaves the pattern of motion unchanged, but yields elevated tissue stresses all along the margin, consistent with the outcome of laser ablation experiments. (**C**) A model with active stresses set to the negative of the passive stress from **A**. This leaves the passive stress unchanged but the tissue stress vanishes (at odds with the outcome of laser ablation experiments, which reveal localized tissue strains at the margin). (**D**) Motion driven by active convergent extension of the prospective primitive streak (represented here as radially symmetric region centered on the posterior margin, corresponding to an intermediate stage in the formation of the primitive streak). Notice that the pattern of motion forms four vortices, at odds with motion observed in the epiblast. (**E, F**) show the effect of non-uniform tissue viscosity (indicated by gray levels, with darker levels indicating higher viscosity), with the same active stress pattern as in **D** (to within a scaling factor to produce velocities of the same magnitude). The viscosity is ten times higher in the EE than in the EP in **E**, and ten times lower in **F**. Notice that the higher EE viscosity in **E**, acting as confining boundary, yields two vortices, but motion does not propagate into the EE, whereas a lower EE viscosity exacerbates the posterior vortices.

initial tissue border and embryo contour		
r_b	border radius	1.81 mm
r_c	contour radius	0.92 mm
	embryo offset along the A-P axis	-0.11 mm
area changes		
r_e	EP border location	1.14*
w_e	EP border width	0.43*
a_1(8h)	EP expansion	0.27*
a_3(8h)	EE expansion	1.58*
w_b	tissue border width	0.19 mm
a_4(8h)	reduced border expansion	1.06*
r_s	PS location	0.945*
Θ_s	PS angular extent	43º
w_s	PS width	0.13*
a_5(8h)	PS contraction	2.26
t_s	PS contraction onset time	5.1 h
t_s	PS contraction onset time scale	2.0 h
* dimensionless parameters		
active stresses		
w	margin width	0.12 mm
Θ_T	angular extent of the tension gradient	40º
$T_{\max} / \eta$	peak tension/viscosity	2.7 mm/h
t^+	onset time	0.95 h
t^+	onset time scale	2.9 h
t^-	decay time scale	8.3 h

Table S1. Model parameters for the synthetic embryo.
The parameter values in this table were used to simulate the synthetic embryo of Fig. S3 and Movie S6, as described in the Supplementary Text.

Movie S1. PIV analysis of a single memGFP embryo cultured *ex vivo*.
Left: Time-lapse movie of a memGFP transgenic embryo (acquisition every 6 min for 10 h) overlaid with trajectories reconstructed by PIV (top; 2 h sliding window) and automatically identified prospective primitive streak (magenta) and EP (green) territories (bottom).
Right: Deformation map. Colors show area changes (blue, expansion; red; contraction) in the initial (top) and current (bottom) configurations of the tissue.

Movie S2. Spatiotemporal registration of 6 control embryos into a reference average embryo.
Time-lapse movies of $n = 6$ memGFP transgenic embryos (acquired every 6 min and registered from $t = t_0$ to $t = t_0 + 8$ h) overlaid with automatically identified prospective primitive streak (magenta) and EP (green) territories (upper row), and the corresponding trajectories (middle row) and deformation maps (bottom row). The last column shows the average embryo constructed from these individual embryos.

Movie S3. PIV analysis of a single memGFP embryo imaged directly in the egg.
Left: Time-lapse movie of a memGFP transgenic embryo (acquisition every 6 min for 9 h, directly from a windowed egg) overlaid with trajectories (top; 2 h sliding window) and automatically identified prospective primitive streak (magenta) and EP (green) territories (bottom).
Right: Deformation map. Colors show area changes (blue, expansion; red; contraction) in the initial (top) and current (bottom) configurations of the tissue.

Movie S4. Analysis of tissue flows in the average embryo.
From left to right: Deformation map, velocity field decomposed into divergent and rotational components, and apparent forces (negative of the Laplacian of the velocity field).

Movie S5. Quantitative model of gastrulation.
Left: Experimental trajectories and deformation map for the average embryo.
Right: Trajectories and deformation map for the model, as fit to the average embryo. Tissue flow in the model is driven by area changes, taken from experiment, and active tensions along the margin (represented by a magenta line for legibility; the margin has a finite width as in Movie S6).

Movie S6. Synthetic model of gastrulation.
Top: time evolution of EE expansion (left, blue), areal contraction of the prospective primitive streak (center, red), and tension along the margin (right, magenta) as a function of space and time used to build a synthetic model of gastrulation. Patterns of areal expansion and contraction, defined relative to the initial configuration of the tissue (as displayed in Fig. S3A), are shown here in its current configuration, where they take effect. Notice in particular that the initially crescent-shaped prospective primitive streak (cf. Fig. S3A) has undergone substantial convergent extension before areal contraction sets in.
Bottom: the resulting trajectories (left) and deformation map (right).

Movie S7. Estimation of tissue strain using UV-laser cuts in control embryos.
Left: Time-lapse movie of a control embryo imaged for 6 h, overlaid with automatically detected margin (dashed line) and apparent forces (arrows), used to position the cuts.
Right: 250 μm laser cuts were then sequentially performed in the posterior margin (red square), anterior margin (green square), and EP (blue square) . Note the anisotropic relaxation at the margin but not in the EP.

Movie S8. Formation of a large-scale supracellular actomyosin ring at the margin.
Time-lapse movie of a *hUbc:Lifeact-NeonGreen_ires_tdTomato-Myl9* transgenic embryo (acquisition every 6 min for 8 h, tdtomato-Myl9 only). Only the right side has been imaged (tiled and stitched), with a 40x objective. The red and blue boxes show higher magnification at the posterior and anterior margin, respectively. Red arrows point at supracellular MyosinII cables progressively developing from the posterior and to the anterior margin of the embryo. The last image is a projection of the last 10 time points to reveal tissue flows.

Movie S9. MyosinII dynamics and concomitant cell behavior at the margin.
Time-lapse movie of a *hUbc:Lifeact-NeonGreen_ires_tdTomato-Myl9* transgenic embryo (acquisition every 6 min for 90 min, tdtomato-Myl9 only) at the anterior and posterior margin (upper and lower panel respectively). A few cells have been tracked (colored dots and masks) to highlight i) the tangential extension of supracellular myosin cables and concomitant cell elongation and oriented division, at the anterior margin; ii) contraction of supracellular myosin cables and cell apical surface at the posterior margin.

Movie S10. Cell dispersion in control and drug-treated embryos.
Time-lapse movie of memGFP transgenic embryos (acquisition every 5 min for 90 min) in control, HU only, HU+Q-VD-OPh, and Q-VD-OPh only, highlighting the effect of cell division and/or apoptosis inhibition on cell rearrangements and subsequent cell dispersion as revealed by segmenting columns of cells (colored masks). Note that whereas HU alone stabilizes epithelial toplogy it induces apoptosis-mediated extrusion of epithelial cells. In contrast, the combination of HU and Q-VD-OPh prevents cell extrusion and greatly stabilizes epithelial topology, whereas Q-VD-OPh only has no noticeable effect on its own on epithelial topology.

Movie S11. Spatiotemporal registration of 5 HU+Q-VD-OPh treated embryos into an average embryo.
Time-lapse movies of memGFP transgenic embryos treated with HU+Q-VD-OPh (acquired every 6 min and registered from $t = t_0$ to $t = t_0 + 8$ h) overlaid with automatically detected EP territory (green; upper row), and the corresponding trajectories (middle row) and deformation maps (bottom row). The last column shows the average embryo constructed from these individual embryos.

Movie S12. Analysis of tissue flows in HU+Q-VD-OPh- treated embryos.
From left to right: Deformation map, velocity field decomposed into divergent and rotational components, and apparent forces (negative of the Laplacian of the velocity field).

Movie S13. Estimation of tissue strain using UV-laser cuts in HU+Q-VD-OPh treated embryos.
Left: Time-lapse movie of a HU+Q-VD-OPh-treated embryo imaged for 6 h, , overlaid with automatically detected margin (dashed line) and apparent forces (arrows), used to position the cuts
Right: 250 μm laser cuts were then sequentially performed in the posterior margin (red square), anterior margin (green square), and EP (blue square). Note the anisotropic relaxation at the margin but not in the EP, as in a control embryo, whereas the apparent forces (negative of the Laplacian of the velocity field) is greatly reduced (compare with Movie S7), arguing for an increase in viscosity.

Movie S14. Response to altered boundary conditions.
Predictions from the synthetic model for the response to centered (left) and off-centered (right) cuts that generate a new tissue border, alongside with the experimental response following a laser cut. Top row: schematic of experiment and time-lapse movie of memGFP embryo, overlaid with automatically identified prospective primitive streak (magenta) and EP (green) territories. Middle row: rotational component of the velocity field. Bottom row: deformation map.

Supplementary references

22. Y. Sato *et al.*, *PLOS ONE*. **5**, e12674 (2010).
23. G. B. Blanchard *et al.*, *Nat. Methods*. **6**, 458–464 (2009).
24. M. Kass, A. Witkin, D. Terzopoulos, *Int. J. Comput. Vis.* **1**, 321–331 (1988).
25. J. Schindelin *et al.*, *Nat. Methods*. **9**, 676–682 (2012).
26. P. Thévenaz, U. E. Ruttimann, M. Unser, *IEEE Trans. Image Process. Publ. IEEE Signal Process. Soc.* **7**, 27–41 (1998).
27. D. Heller *et al.*, *Dev. Cell*. **36**, 103–116 (2016).
28. Icy: an open bioimage informatics platform for extended reproducible research. - PubMed - NCBI, (available at https://www.ncbi.nlm.nih.gov/pubmed/22743774).
29. B. Aigouy, D. Umetsu, S. Eaton, *Methods Mol. Biol. Clifton NJ*. **1478**, 227–239 (2016).
30. M. Raffel, C. E. Willert, steven wereley, J. Kompenhans, *Particle Image Velocimetry: A Practical Guide* (Springer Science & Business Media, 2007).
31. A. J. Chorin, J. E. Marsden, *A Mathematical Introduction to Fluid Mechanics* (Springer-Verlag, New York, ed. 3, 1993; //www.springer.com/us/book/9780387979182), *Texts in Applied Mathematics*.
32. R. H. Dillon, in *Mathematical Models for Biological Pattern Formation*, P. K. Maini, H. G. Othmer, Eds. (Springer New York, 2001), *The IMA Volumes in Mathematics and its Applications*, pp. 39–57.
33. W. H. Press, S. A. Teukolsky, W. T. Vetterling, B. P. Flannery, Numerical Recipes 3rd Edition: The Art of Scientific Computing.
34. B. Aigouy *et al.*, *Cell*. **142**, 773–786 (2010).
35. E. A. Zamir, B. J. Rongish, C. D. Little, *PLoS Biol.* **6**, 1–9 (2008).
36. F. Hecht, *J. Numer. Math.* **20**, 251–266 (2013).
37. H. Acloque *et al.*, *Dev. Cell*. **21**, 546–558 (2011).
38. V. Fleury, *Organogenesis*. **2**, 6–16 (2005).